iScience

CellPress
OPEN ACCESS

Article

Deep-Breathing Honeycomb-like Co-N_x-C Nanopolyhedron Bifunctional Oxygen Electrocatalysts for Rechargeable Zn-Air Batteries

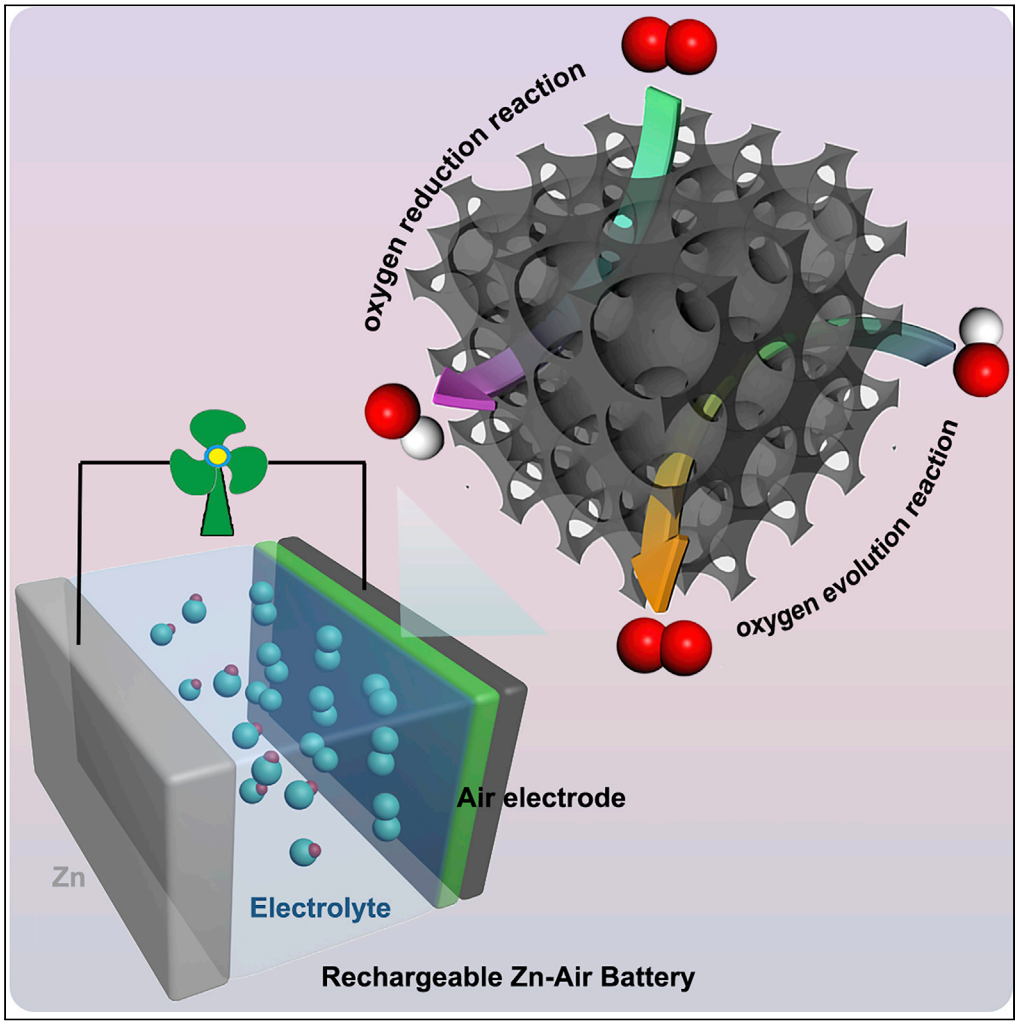

Zhaoqiang Li, Gaopeng Jiang, Ya-Ping Deng, ..., Yongfeng Hu, Shun Wang, Zhongwei Chen

shunwang@wzu.edu.cn (S.W.)
zhwchen@uwaterloo.ca (Z.C.)

HIGHLIGHTS

A deep-breathing oxygen electrocatalyst with highly dispersed active sites was built

Sculpturing ordered macropores in MOF derivatives enables fast mass transport

The honeycomb-like Co-N_x-C nanopolyhedron worked well in rechargeable Zn-air battery

Li et al., iScience *23*, 101404
August 21, 2020
https://doi.org/10.1016/j.isci.2020.101404

iScience

CellPress
OPEN ACCESS

Article

Deep-Breathing Honeycomb-like Co-N_x-C Nanopolyhedron Bifunctional Oxygen Electrocatalysts for Rechargeable Zn-Air Batteries

Zhaoqiang Li,[1,2] Gaopeng Jiang,[2] Ya-Ping Deng,[2] Guihua Liu,[2] Dezhang Ren,[2] Zhen Zhang,[2] Jianbing Zhu,[2] Rui Gao,[2] Yi Jiang,[2] Dan Luo,[2] Yanfei Zhu,[2] Dai-Huo Liu,[2] Altamash M. Jauhar,[2] Huile Jin,[1] Yongfeng Hu,[3] Shun Wang,[1,*] and Zhongwei Chen[2,4,*]

SUMMARY

Metal organic framework (MOF) derivatives have been extensively used as bifunctional oxygen electrocatalysts. However, the utilization of active sites is still not satisfactory owing to the sluggish mass transport within their narrow pore channels. Herein, interconnected macroporous channels were constructed inside MOFs-derived Co-N_x-C electrocatalyst to unblock the mass transfer barrier. The as-synthesized electrocatalyst exhibits a honeycomb-like morphology with highly exposed Co-N_x-C active sites on carbon frame. Owing to the interconnected ordered macropores throughout the electrocatalyst, these active sites can smoothly "exhale/inhale" reactants and products, enhancing the accessibility of active sites and the reaction kinetics. As a result, the honeycomb-like Co-N_x-C displayed a potential difference of 0.773 V between the oxygen evolution reaction potential at 10 mA cm^{-2} and the oxygen reduction reaction half-wave potential, much lower than that of bulk-Co-N_x-C (0.842 V). The rational modification on porosity makes such honeycomb-like MOF derivative an excellent bifunctional oxygen electrocatalyst in rechargeable Zn-air batteries.

INTRODUCTION

The extensive demand for renewable and clean energy spurs the blooming development of advanced energy storage and conversion techniques (Xu et al., 2016; Huang et al., 2019; Zhang et al., 2019a; Jiang et al., 2016). Rechargeable metal-air batteries, in which metal serves as the anode, and electrocatalyst-containing gas diffusion layer as the cathode, are drawing increasing attention owing to their low price, high theoretical energy density, and environment friendliness (Lee et al., 2011; Jiang et al., 2018; Luo et al., 2019; Cheng et al., 2017). Particularly, rechargeable Zn-air batteries (RZABs), with a high theoretical volumetric energy density of 6,163 Wh L^{-1}, have been regarded as one of the most promising next-generation energy storage and conversion devices (Zhang et al., 2019b; Yin et al., 2017; Lai et al., 2018; Wang et al., 2018b; Deng et al., 2020). However, the commercialization of RZABs is still hindered by the unsatisfied bifunctionality and poor cyclability, which is originated from the sluggish reaction kinetics and inferior stability for both oxygen reduction reaction (ORR) and oxygen evolution reaction (OER) (Cao et al., 2012; Tsvetkov et al., 2016; Li et al., 2018; Wang et al., 2017b, 2018a; Liu et al., 2015). Rational engineering on bifunctional oxygen electrocatalysts seems to be urgent for the development of RZABs.

Recently, metal organic framework (MOF) derivatives have drawn great attention for their feasibilities as bifunctional oxygen electrocatalysts (Zhang et al., 2017; Chen et al., 2019; Tao et al., 2017; Wang et al., 2017a; Li et al., 2020). With proper treatments, MOFs can be controllably transformed into metal species-embedded carbon architectures (Li et al., 2017, Li and Yin, 2018; Guan et al., 2016; Lee et al., 2016; Mukherjee et al., 2018; Meng et al., 2017) and are commonly used as bifunctional oxygen electrocatalysts (Cheng et al., 2019b; Wan et al., 2018; Wang et al., 2016; Xia et al., 2016; Huang et al., 2017). As the most popular method of fabricating MOF-derivatives, the direct calcination of original solid MOFs often leads to the formation of MOF-derivatives with narrow pore channels (Miao et al., 2018; He et al., 2019; Li and Yin, 2015a; Dou et al., 2016, Dou et al., 2019; Xuan et al., 2019), which are easily blocked by electrolyte when used in oxygen electrocatalysis. Hence, oxygen molecules will not be able to reach the active sites

[1]College of Chemistry and Materials Engineering, Institute of New Materials and Industrial Technologies, Wenzhou University, Wenzhou, Zhejiang 325035, P. R. China

[2]Department of Chemical Engineering, Waterloo Institute for Nanotechnology, Waterloo Institute for Sustainable Energy, University of Waterloo, Waterloo, ON N2L 3G1, Canada

[3]Canadian Light Source, University of Saskatchewan Saskatoon, Saskatchewan S7N 2V3, Canada

[4]Lead Contact

*Correspondence: shunwang@wzu.edu.cn (S.W.), zhwchen@uwaterloo.ca (Z.C.)

https://doi.org/10.1016/j.isci.2020.101404

inside the carbon matrix (Hou et al., 2019). This phenomenon makes the active sites difficult to "breath," especially for those buried deep inside (Liu et al., 2019; Cheng et al., 2019a; Wang et al., 2018c), corresponding to a very low utilization of active sites. To alleviate this issue, some electrocatalysts with abundant micro/mesopores or interior hollows were synthesized to achieve better mass transport (Lin et al., 2017; Zhong et al., 2018). However, the micro/mesoporous channels are often disordered, and the hollow structures are often airtight, thus the mass transfer between inside and outside of the particles are still not satisfactory (Xu et al., 2018; Wang et al., 2018e; Lu et al., 2019). More efforts are needed to further eliminate the mass transfer barrier so as to obtain more effective bifunctional electrocatalysts.

Constructing interconnected ordered macroporous channels throughout catalyst would be beneficial to unblock the mass transfer barrier so as to obtain effective deep-breathing bifunctional oxygen electrocatalyst. The interconnected ordered macropores not only can deliver more effective mass transport than the traditional micro/mesoporous disordered channels but also can expose a large number of active sites. Thus, it indisputably enhances the reaction kinetics for both OER and ORR and enables much enhanced electrocatalytic activities than the traditional bulk electrocatalysts (Hu et al., 2012; Cui et al., 2018). Fabricating interconnected ordered macroporous channels inside MOFs-derived bifunctional oxygen electrocatalyst is highly desired, but challenging. In this work, we achieved this design by fabricating a honeycomb-like superstructure. Different from previous reports that used solid MOFs as precursor, a delicate MOF with pre-sculptured interconnected macropores was employed instead. After a simple calcination process, an exquisite bifunctional oxygen electrocatalyst with inherited honeycomb-like morphology was obtained, with highly dispersed Co-N_x-C active sites homogenously distributed in N-doped carbon frame. The interconnected macropores throughout the catalyst, worked just like alveolus, supporting the flash transfer of reactants and products in the catalyst, even deep inside the polyhedral particles. All active sites can smoothly "inhale" OH^- and "exhale" the generated O_2 during OER, whereas "inhale" O_2 and "exhale" the generated OH^- during ORR. A "deep breathing" bifunctional electrocatalyst, with all active sites "breathing" without any obstacles, was achieved with the aid of interconnected macropores. Besides the flash mass transfer process, the designed electrocatalyst exhibits a lot of advantages that facilitate the electrochemical processes, such as exposed large amounts of active sites, fast charge transfer, and excellent durability due to the conductive robust carbon frame. As a result, the honeycomb-like Co-N_x-C exhibited outstanding bifunctional capability and good durability when employed as air electrode electrocatalyst for in RZABs.

RESULTS AND DISCUSSION

Figure 1 shows the fabrication process of honeycomb-like ZIF-67 and its derived honeycomb-like Co-N_x-C electrocatalysts. Uniform polystyrene (PS) nanoparticles with size 180 nm were orderly assembled into bulk matrix through centrifuge method (Figure S1). After immersing PS template into $Co(NO_3)_2$ solution, the voids between PS spheres were first filled with $Co(NO_3)_2$, which will provide metal ions during the nucleation of ZIF-67. The subsequent soaking of PS/$Co(NO_3)_2$ into 2-MeIM methanol solution introduces organic ligand into PS templates, initiating the reaction between $Co(NO_3)_2$ and 2-MeIM. The ZIF-67 starts to nucleate and grow up, finally leading to the formation of ZIF-67 polyhedrons inside the PS templates. That is, the ZIF-67 single crystal polyhedrons with ordered PS particles inside were formed. After the removal of PS using DMF, honeycomb-like ZIF-67 single-crystal polyhedrons containing closely neighbored macropores were obtained, which was then calcined in tube furnace. During the calcination process, the ZIF-67 decomposed slowly, during which organic ligands were transformed into N-doped carbons and the atomically dispersed cobalt ions in the matrix were transformed into highly dispersed Co-N_x-C units. The activity of electrocatalyst was optimized by different calcination temperatures, with samples obtained under 500°C, 600°C, and 700°C named as Honeycomb-500, Honeycomb-600, and Honeycomb-700, respectively.

Scanning electron microscopy (SEM) and transmission electron microscopy (TEM) were first employed to investigate the microstructure of the obtained samples. Under normal circumstances, cobalt ions coordinate with 2-MeIM to form a solid single-crystal particle with a typical polyhedral morphology (Figure S2). For the crystal growth of ZIF-67 inside PS template, it proceeds only in the interconnected voids of PS template, finally leading to ZIF-67 single-crystal polyhedrons with closely neighbored macropores inside after removal of PS templates, which exhibits a honeycomb-like morphology. As shown in Figure 2A, the honeycomb-like ZIF-67 single crystals exhibit a typical polyhedral morphology with particle size of about 0.8–4 μm and macropores in the particle. This is further confirmed by TEM observation (Figure 2B), which clearly

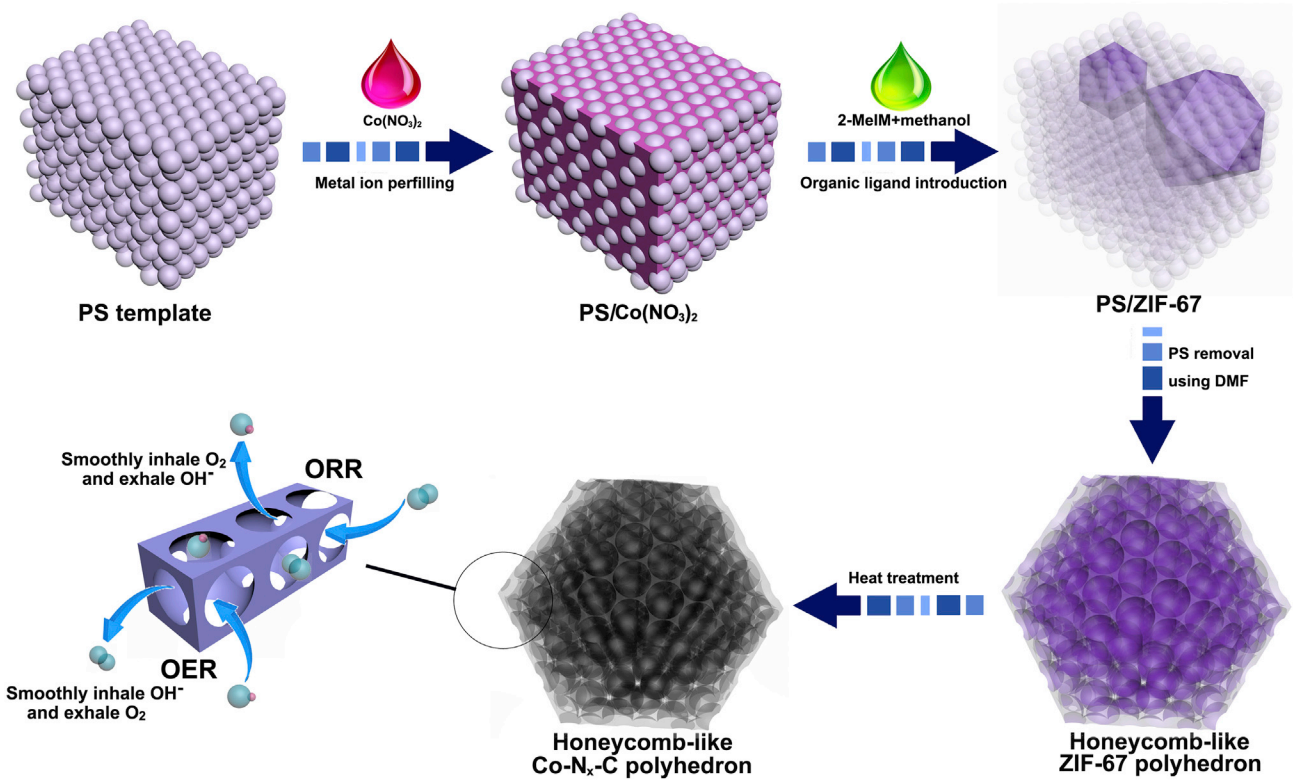

Figure 1. Schematic Illustration of the Construction of the MOFs-Derived Honeycomb-like Co-N_x-C Superstructures

shows the presence of closely neighbored macropores of 180 nm throughout the ZIF-67 single crystal. In the X-ray powder diffraction (XRD) pattern (Figure 2C), several sharp diffraction peaks located at 10.5°, 12.5°, 18.3° etc. are observed, which is consistent with the XRD pattern of previously reported ZIF-67 (Li et al., 2016). This demonstrates that the sculpture of interconnected macropores inside the ZIF-67 does not change the crystallinity of ZIF itself. In the nitrogen adsorption-desorption isotherms (Figure S3A), the bulk ZIF-67 exhibits a typical type I behavior, with a large adsorption capacity in the low-pressure region around 0, which indicates the existence of large amount of micropores. In contrast, for the honeycomb-like ZIF-67 (Figure 2D), similar isotherms were obtained except for an additional adsorption capacity in the high-pressure region, revealing the presence of macropores. From the inset of Figure 2D, the honeycomb-like ZIF-67 exhibits almost the same micropore distribution curve as bulk ZIF-67 (Figure S3B), further confirming that the sculpturing of macropores inside ZIF-67 does not destroy the microstructure of ZIF-67.

When calcined under high temperature, the organic ligand of ZIF-67 decomposed into nitrogen-doped carbon materials, whereas metal species was transformed into Co-N_x-C units. As shown in Figures 3A–3C and Figure S4, the honeycomb-like Co-N_x-C superstructures inherited the classic polyhedron configuration of honeycomb-like ZIF-67 with interconnected macropores of 130 nm. The shrinkage of particles as well as the macropores after calcination is commonly observed in MOF-derivatives or other metal organic derivatives, which is mainly ascribed to the decomposition of organic species (Meng et al., 2017; Hou et al., 2019). As shown in the high-magnification SEM images of Figures 3B, 3C, and S4, the carbon walls between the two macropores are very thin, which is beneficial for fast mass transportation for the active sites inside the carbon walls during electrochemical reactions. The honeycomb-like configuration of Co-N_x-C was further verified by TEM observations (Figures 3D and 3E), which clearly reveals the presence of 130-nm interconnected macropores inside the particle. The further magnified TEM images (Figures 3F and S5A) show that cobalt nanoparticles with size of 2–10 nm are highly dispersed on typical layer-structured carbon frame. The nitrogen-doped carbon frame will serve as not only robust substrate for active sites but also conductive medium for electron transfer during electrochemical reactions, thus playing a crucial role in the designed electrocatalyst. As shown in Figure S5B of the high-resolution TEM image, the lattice fringes were clearly observed,

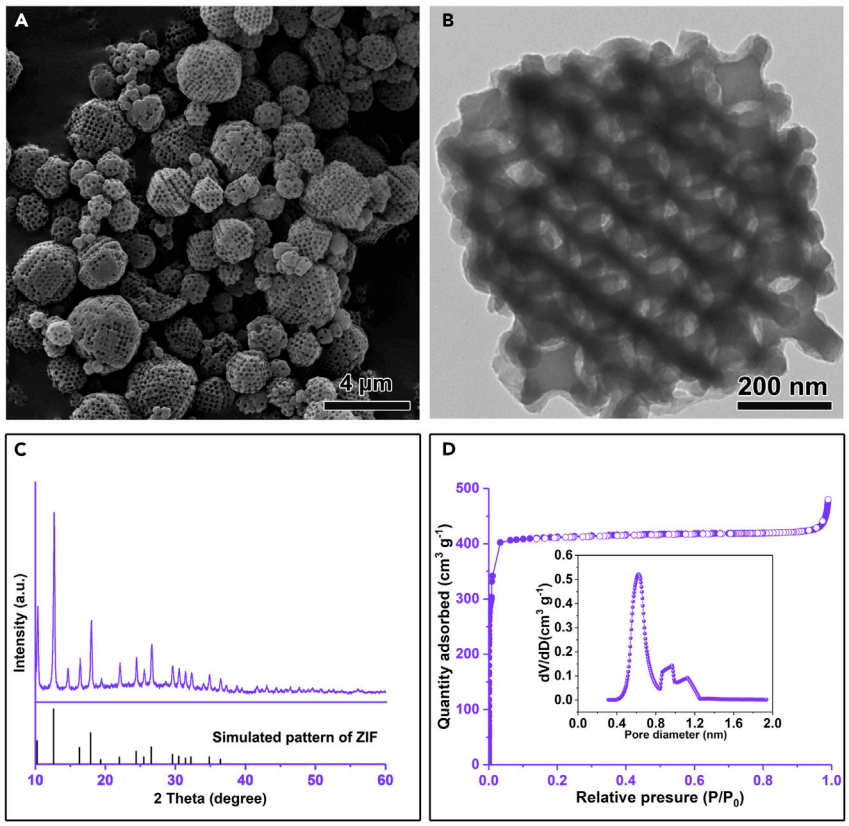

Figure 2. Characterizations for the Honeycomb-like 3DOM ZIF-67

(A–D) (A) SEM image, (B) TEM image, (C) XRD pattern, and (D) N_2 adsorption-desorption isotherms and pore size distribution (inset) results of the honeycomb-like ZIF-67.

which were measured to be 0.2 nm, corresponding well with (111) plane of cobalt (Li et al., 2016). In the mapping results (Figure 3G), the Co, C, and N elements homogenously distributed along the profiles of honeycomb-like Co-N_x-C nanoparticles, which is consistent with the aforementioned TEM observations. According to the N_2 adsorption-desorption tests, Honeycomb-600 shows a higher specific surface area (243.4 m^2 g^{-1}) and a larger total pore volume (0.365 cm^3 g^{-1}) than that of Bulk-600 (specific surface area of 226.9 m^2 g^{-1} and pore volume of 0.143 cm^3 g^{-1}) (Figure S6). The obvious increase of total pore volume may result from the sculpturing of interconnected macropores inside MOF-derivatives (Yang et al., 2017; Park et al., 2016; Zhong et al., 2017). The sculptured interconnected macropores inside the MOFs-derived Co-N_x-C expose more active sites for OER and ORR reactions, as well as provide unblocked highways for mass transportation during electrochemical reactions, thus expecting to display much enhanced electrocatalytic activities than the bulk Co-N_x-C (Figure S7).

The phase components were further confirmed by the XRD technique. To investigate the influence of calcination temperature on the performance of Co-N_x-C, the honeycomb-like Co-N_x-C samples with different calcination temperatures (500°C, 600°C and 700°C) were also synthesized, named as Honeycomb-500, Honeycomb-600, and Honeycomb-700, respectively. For the XRD patterns of honeycomb-like Co-N_x-C samples (Figure 4A), a broad diffraction peak located at 25° can be observed, which is due to the existence of carbon materials (Li and Yin, 2015a, 2015b). Apart from this, three peaks located at 44.2°, 51.5°, and 75.9° can also be detected, which match well with the (111), (200), and (220) planes of cobalt (PDF# 89-4307). This result confirms the small nanoparticles on the carbon matrix to be cobalt, which is consistent with the result of lattice fringe observation in high-resolution TEM images. Although exhibiting same peak positions, the honeycomb-like Co-N_x-C samples with different calcination temperatures show different peak intensities. With the increase of calcination temperature, the peak intensities show an increasing trend, indicating better crystallinity of cobalt nanoparticles.

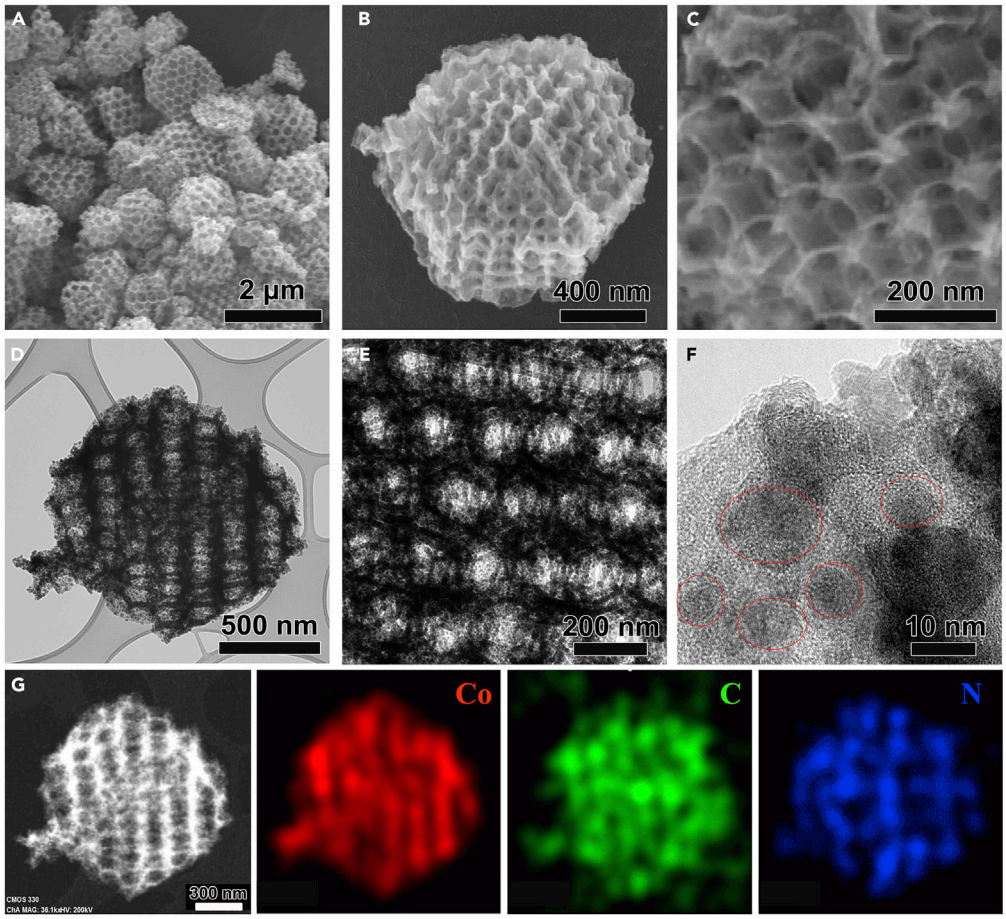

Figure 3. Morphological Characterizations of the Honeycomb-600

(A–G) (A–C) SEM images, (D–F) TEM images, and (G) energy-dispersive X-ray mapping results of the Honeycomb-600 nanostructure. See also Figures S4 and S5.

X-ray photoelectron spectroscopy was then conducted to reveal the chemical compositions and bonding configurations of the samples with different heat treatments. In the survey spectra (Figures S8–S10), the Honeycomb-600 sample exhibited a much stronger N peak than Honeycomb-500 and Honeycomb-700, indicating a relatively higher N content. The nitrogen in the final catalyst comes from two sources, i.e., the pristine organic linkers and NH_3 treatment. With the increase of heating temperature, the N from organic linkers decreases, whereas that from NH_3 treatment increases, finally leading to an optimized high N content in the Honeycomb-600 sample. This is also confirmed by the calculated elemental compositions (Table S1), which shows a much higher N content of Honeycomb-600 (13.58 atom %) than that of Honeycomb-500 (6.43 atom %) and Honeycomb-700 (6.35 atom %). In N 1s spectrum (Figure 4B), a fitted peak located at 399.1 eV can be observed, indicating the existence of Co-N_x units (Tang et al., 2017). The other three peaks located at 398.3, 400.2, and 401.1 eV correspond to pyridinic N, pyrrolic N, and quaternary N, respectively. It is reported that the nitrogen-based units (Co-N_x-C and N-C) are effective active sites for ORR and OER (Yan et al., 2017; Wang et al., 2018d; Luo et al., 2018), so the relatively higher N content of Honeycomb-600 may portend better ORR and OER bifunctional activities. As shown in Figure 4C of the Co 2p spectrum for Honeycomb-600, two fitted peaks at 780.8 and 796.4 eV can be observed, which can be assigned to Co $2p_{3/2}$ and Co $2p_{1/2}$ of Co-N_x, whereas the peaks at 778.5 and 793.3 eV are related to Co $2p_{3/2}$ and Co $2p_{1/2}$ of metallic Co(0). X-ray absorption near-edge structure spectra were collected to further confirm the chemical state of the elements (Ravel and Newville, 2005). As shown in the Co K-edge absorption spectra (Figure 4D), the position of absorption edge for Honeycomb-600 is close to that of reference CoO, implying a higher chemical valence than cobalt foil, which is ascribed to the strong coupling between cobalt and carbon through Co-N_x coordination (Qiao et al., 2019). More importantly, the peak area of

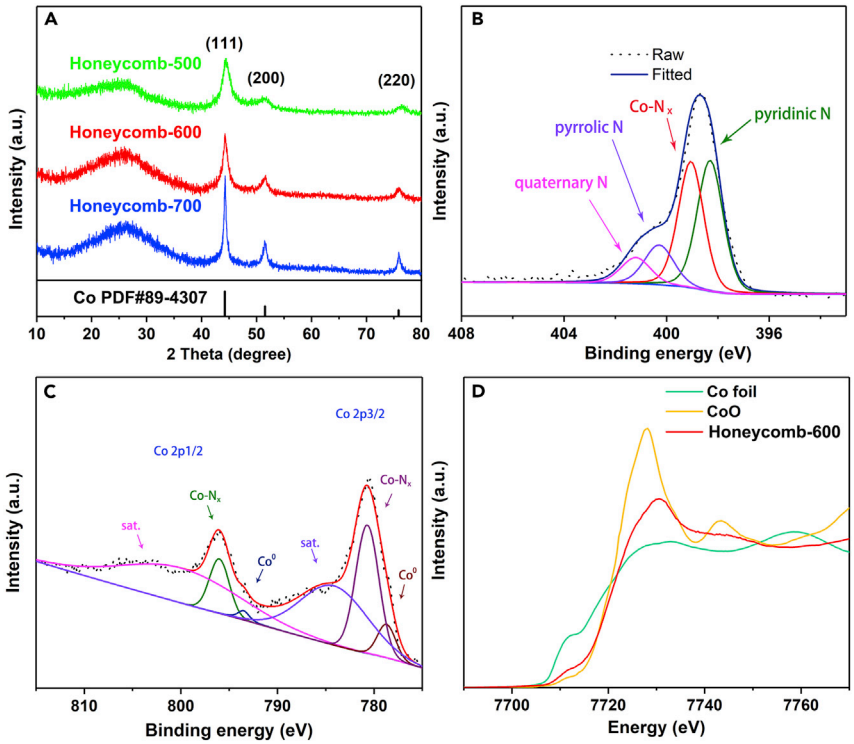

Figure 4. Composed Characterization of the Honeycomb-like Co-N_x-C Samples

(A–C) (A) XRD patterns of honeycomb-like Co-N_x-C samples. High-resolution (B) N 1s spectrum and (C) Co 2p spectrum the Honeycomb-600 sample.

(D) Co K-edge X-ray absorption near-edge structure spectra of three samples. See also Table S1.

Honeycomb-600 is much lower than that of CoO, revealing that it is more electron rich compared with CoO. This also implies the existence of Co-N_x coordination because nitrogen is less electron negative, which draws less electrons than oxygen and results in smaller peak area.

The bifunctional electrocatalytic activities of the electrocatalysts were evaluated through the linear sweep voltammetry (LSV) technique in 0.1 M KOH solution. The commercial Pt/C and Ir/C samples were also tested under the same condition as performance benchmarks. As shown in Figure 5A, for the Bulk-600 catalyst, the onset potential (E_{onset}) was measured to be 0.879 V. However, for the Honeycomb-600 catalyst which contains interconnected macropores inside, the E_{onset} was positively enhanced to 0.901 V. To reveal the influence of heat treatment temperature on the electrocatalyst activities, Honeycomb-500 and Honeycomb-700 were also tested under the same condition. As shown in Figure 5A, Honeycomb-500 exhibited an E_{onset} of 0.866 V, inferior to that of Honeycomb-600, which may be owing to the lower degree of graphitization under lower calcination temperature. As for Honeycomb-700 obtained under 700°C calcination, more Co-N_x-C units with high ORR activities were transformed into cobalt nanoparticles, and small cobalt nanoparticles also agglomerated each other to form bigger cobalt nanoparticles, which was evidenced by the big particles with size greater than 10 nm in the TEM image of Honeycomb-700 (Figure S11). The agglomeration of small cobalt particles always accompanied by the corrosion of the N-doped carbons between the original small particles, which was also indicated by the drastic decrease of nitrogen content from 13.58 atom % to 6.35 atom % (Table S1). The agglomeration of small cobalt particles and the corrosion of N-doped carbon resulted in the loss of active sites, finally leading to poorer ORR activity than that of Honeycomb-600.

Moreover, the Honeycomb-600 electrocatalyst exhibited a half-wave potential ($E_{1/2}$) of 0.837 V, which is much better than that of Bulk-600 (0.802 V), Honeycomb-500 (0.815 V), and Honeycomb-700 (0.801 V), further demonstrating the superior ORR activity of Honeycomb-600 electrocatalyst. The LSV curves measured at different rotating speeds were further measured to evaluate the electron transfer kinetics

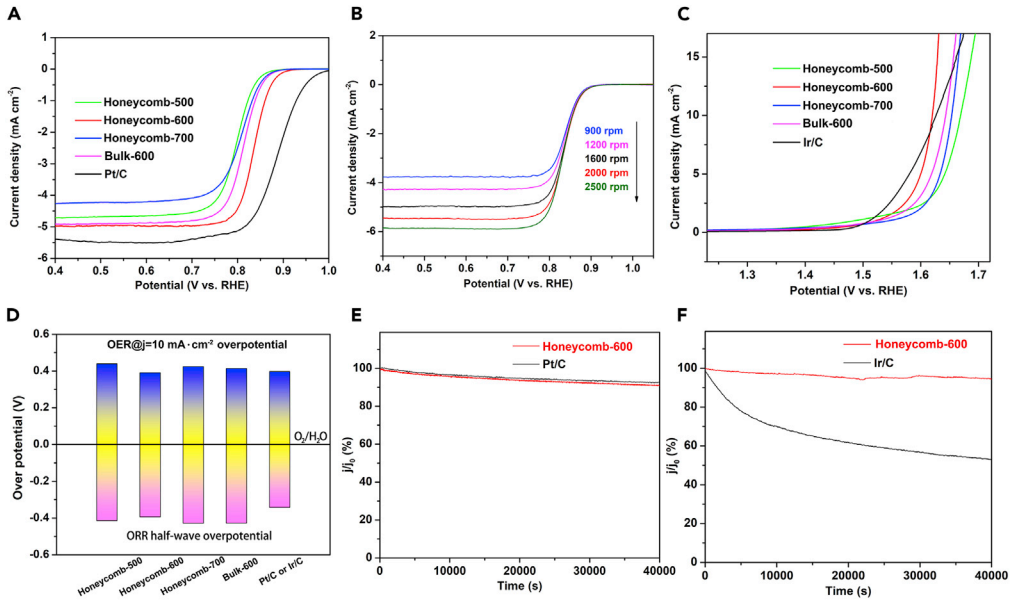

Figure 5. Electrocatalytic Activities of the Samples

(A) ORR LSV curves of the samples.

(B) LSV curves of Honeycomb-600 at various rotating speeds.

(C) OER LSV curves of the samples.

(D) Overpotentials of ORR and OER for different samples.

(E) ORR chronoamperometric response of Honeycomb-600 at 0.71 V.

(F) OER chronoamperometric response of Honeycomb-600 and Ir/C at 1.65 V.

See also Figures S12–S14.

of the Honeycomb-600. As shown in Figure 5B, the Honeycomb-600 shows diffusion-limited currents under different rotating speeds, with an increasing current density when the rotating speed increases. The corresponding Koutecky-Levich (K-L) plots at different potentials (Figure S12) display good linearity with an electron transfer number calculated to be 3.8, revealing fast electron-transfer kinetics of the Honeycomb-600. Furthermore, the Honeycomb-600 catalyst exhibited a Tafel slope of 60.4 mV dec^{-1} (Figure S13A), smaller than that of Bulk-600 without macropores (66.5 mV dec^{-1}) and even comparable with that of Pt/C (60.3 mV dec^{-1}), indicating a rapid ORR kinetics. The much better reaction kinetics of Honeycomb-600 electrocatalyst was further revealed by the kinetic current density (J_k) calculated by the K-L equation. For the Honeycomb-600 sample, a J_k of 9.45 mA cm^{-2} at 0.8V was displayed (Figure S13B), which is much larger than that of Bulk-600 (4.00 mA cm^{-2}). The oxygen evolution activities were further investigated in N_2-saturated 0.1 M KOH solution. Similar to ORR activities, Honeycomb-600 electrocatalyst displayed a superior OER activity (Figure 5C). It can generate a current density of 10 mA cm^{-2} at a potential of 1.610 V versus reversible hydrogen electrode, which is much lower than that of Bulk-600 (1.644 V), Honeycomb-500 (1.669 V), and Honeycomb-700 (1.654 V) and even better than that of Ir/C (1.627 V). The smaller Tafel slope of Honeycomb-600 (85.9 mV dec^{-1}) further confirms the better OER reaction kinetics than other catalysts (Figure S14). The potential difference (ΔE) between the OER potential at 10 mA cm^{-2} ($E_{j=10}$) and the ORR half-wave potential ($E_{1/2}$) is always employed to evaluate the bifunctional oxygen capability of electrocatalysts, with a smaller ΔE indicating a better electrocatalytic bifunctionality. As shown in Figure 5D, Honeycomb-600 displayed a ΔE of 0.773 V, which is much smaller than that of Bulk-600 without macropores (0.842 V) and other honeycomb-like Co-N_x-C catalysts, further demonstrating a critical role of ordered macropores played in OER and ORR processes.

The sculpture of interconnected macropores inside the MOF-derivatives leads to rapid mass transportation for OER and ORR reactions, during which the reactants can be rapidly transported onto active sites and at the same time the products can be effectively transported out through these channels, making the active sites buried deep inside available for electrochemical reactions. Electrochemical impedance spectroscopy was then employed to provide some evidences about the enhancement on mass transportation by interconnected macropores. Typically, electrochemical impedance spectrum consists of a

semicircle in the high-medium-frequency region and a sloping lane in the low-frequency region, in which the sloping lane is related to the mass transport of reactants (Yuan et al., 2016; Wu et al., 2019). As shown in Figure S15, the Honeycomb-600 sample with interconnected macropores displayed a deeper sloping lane in low-frequency region than Bulk-600, indicating a better mass transport capability of the Honeycomb-600. Furthermore, the Warburg coefficient (σ) of the Honeycomb-600 was calculated to be 165.5 $\Omega\ s^{-0.5}$, much smaller than that of Bulk-600 (399.8 $\Omega\ s^{-0.5}$). Both the deeper sloping lane and the smaller Warburg coefficient of Honeycomb-600 revealed the better mass transport processes than Bulk-600 (Yuan et al., 2016; Wu et al., 2019). This honeycomb-like superstructure with interconnected macroporous channels makes active sites "breathe" more smoothly than the traditional bulk MOF-derivatives during OER and ORR processes, thus leading to a much higher utilization of active sites and much enhanced OER and ORR kinetics.

Besides superior OER and ORR reaction kinetics demonstrated earlier, the electrochemical stabilities of both OER and ORR are also important for their practical application, which was evaluated by chronoamperometric (CA) measurement in 0.1 M KOH for 40,000 s. As shown in Figure 5E, after continuously operating ORR at 0.71 V for 40,000 s, Honeycomb-600 can retain 90.9% of the initial ORR current, which is comparable to that of Pt/C (92.4%), exhibiting an excellent ORR stability. Similarly, a superior stability of OER process was also confirmed by the CA test operating at 1.65 V, presenting a high current retention of 94.4% after 40,000 s, outperforming the commercial Ir/C (53.2%) (Figure 5F). The MOFs-derived honeycomb-like strong carbon frame with high nitrogen doping can effectively prevent the highly dispersed active sites from agglomeration, thus serving as robust and ideal host for active sites with great durability for long cycling. As shown in Figure S16, the honeycomb-like superstructure remains intact after continuous OER or ORR tests, further confirming the excellent structural stability of Honeycomb-600 when acting as bifunctional electrocatalyst for ORR and OER.

Depending on the superior ORR and OER performances, the Honeycomb-600 electrocatalyst was sprayed onto carbon paper to fabricate air electrode for RZABs (Figure 6A). For comparison, commercialized Ir/C and Pt/C were mixed and employed to build a benchmark air electrode. The galvanodynamic discharge and charge curves were first measured to investigate the polarization properties of the batteries under different current densities. As illustrated in Figure 6B, the Honeycomb-600 air electrode exhibited much smaller polarization under various currents than the Pt/C + Ir/C benchmarks, corresponding to better OER and ORR reaction activities. Accordingly, Honeycomb-600 delivered a peak power density of 109.6 mW cm^{-2} at a current density of 156.4 mA cm^{-2} (Figure 6C), also much better that that of Pt/C plus Ir/C catalyst (91.1 mW cm^{-2} at 122 mA cm^{-2}).

The cycling test of the Honeycomb-600 air electrode for RZABs was evaluated by the galvanostatic charge-discharge tests, which was measured under a current density of 10 mA cm^{-2} with 15 min charging and 15 min discharging (Figure 6D). For the commercial Pt/C + Ir/C electrode, a fast decay occurred in the initial cycles, finally exhibiting a limited cyclability of only 35 h. The noble metal particles gradually migrate and agglomerate with each other to form bigger particles, leading to the loss of active sites during continuous cycling. As for Honeycomb-600, the initial discharge-charge voltage gap was measured to be 1.03 V. During the following cycling processes, Honeycomb-600 displayed an ultra-stable cycling performance, remaining at 1.07 V after 100 h (2.16 V for charging and 1.09 V for discharging), displaying good durability for practical application. Last, a mini-fan can be steadily powered by RZABs employing Honeycomb-600 as bifunctional oxygen electrocatalyst, confirming its great potential in practical application (Figure 6E).

All these results reveal Honeycomb-600 to be an excellent bifunctional oxygen electrocatalyst with superior OER and ORR kinetics and outstanding long-cycling stability, which is ascribed to the unique honeycomb-like superstructure that makes electrochemical reaction processes easier and faster. First, the interconnected macroporous channels throughout the electrocatalyst act as unblocked highways for mass transportation of O_2 and OH^-, making the active sites "breathe" smoothly during OER and ORR processes, even for active sites deep inside. This enables a better utilization of active sites for promoted reaction kinetics. Second, the sculpturing of interconnected macropores inside MOF-derivatives exposes large amounts of active sites for OER and ORR, facilitating the electrochemical processes. Third, the nitrogen-doped robust carbon framework with a unique thin-wall structure derived from the honeycomb-like ZIF-67 single-crystal polyhedron not only ensures fast mass transportation inside the carbon walls but also serves as strong matrix for highly dispersed active sites, preventing them from agglomeration so as to

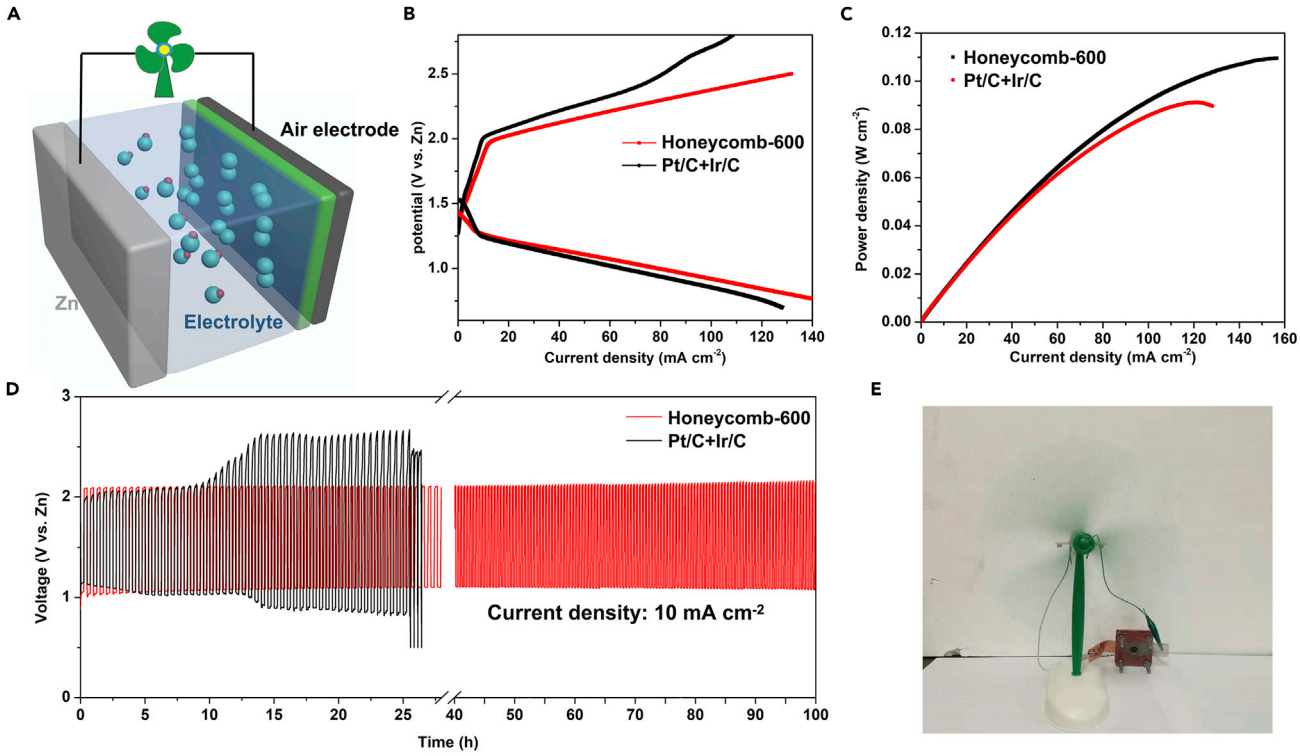

Figure 6. Evaluation of the Rechargable Zn-Air Batteries

(A) A typical system of ZAB.

(B–D) (B) Charging and discharging polarization curves, (C) the corresponding power density plots, and (D) galvanostatic cycling stability of the ZABs fabricated with Honeycomb-600 and Pt/C + Ir/C air electrodes under current density of 10 mA cm^{-2} with 15 min discharging and 15 min charging, respectively.

(E) Demonstration of a zinc-air battery coupled with Honeycomb-600 electrocatalyst to power a mini-fan in ambient atmosphere.

reach long durability when used in ZABs. Besides, the interconnected carbon framework with high nitrogen content provides a three-dimensional conductive highway for charge transfer, further facilitating electrochemical processes.

Conclusions

In summary, a deep-breathing honeycomb-like superstructure with effective Co-N_x-C active sites highly dispersed on a honeycomb-like N-doped polyhedral carbon framework was achieved by simple calcination of a honeycomb-like ZIF-67 single crystal. Inheriting from the honeycomb-like ZIF-67 precursor, the interconnected ordered macroporous channels not only help the fast transportation of O_2 and OH^- to make the active sites "breathe" smoothly during OER and ORR processes but also exposed a large amount of active sites to enable high utilization of active sites for promoted reaction kinetics. As a result, Honeycomb-600 exhibited a high kinetic current density, which is more than twice that of Bulk-600. When evaluated as the air electrode catalyst in a practical ZAB, the Honeycomb-600 output a high peak power density of 109.6 mW cm^{-2}, superior than that of the commercial Pt/C + Ir/C benchmark (91.1 mW cm^{-2}). The excellent bifunctional oxygen electrocatalytic activity is ascribed to the unique honeycomb-like superstructure, which possesses deep-breathing effective Co-N_x-C active sites, fast mass transportation by the interconnected macroporous channels, and quick charge transfer by the highly conductive carbon framework. The combination of interconnected macroporous channels with MOF-derivatives and its demonstration on bifunctional electrocatalyst for RZABs open a new page for MOF-derivatives, demonstrating high potential in other energy devices and other possible applications.

Limitations of the Study

In this study, the PS template was employed for constructing three-dimensional ordered macropores (3DOM) inside the MOF precursors. This PS template is available for MOFs that can be grown under

relatively low temperature (generally below 80°C). However, owing to the low melting point of PS, the PS template may be not suitable for fabrication of 3DOM MOFs that grow in hydrothermal reactions under high temperature. Inspired by this method, other templates, such as silica templates that assembled by silica spheres, could be available for other similar fabrications.

Resource Availability

Lead Contact

Further information and requests for resources and reagents should be directed to and will be fulfilled by the Lead Contact, Zhongwei Chen (zhwchen@uwaterloo.ca).

Materials Availability

This study did not generate new unique reagents.

Data and Code Availability

The published article includes all datasets/code generated or analyzed during this study.

METHODS

All methods can be found in the accompanying Transparent Methods supplemental file.

SUPPLEMENTAL INFORMATION

Supplemental Information can be found online at https://doi.org/10.1016/j.isci.2020.101404.

ACKNOWLEDGMENTS

The authors acknowledge the financial support from the University of Waterloo and Wenzhou University, Natural Sciences and Engineering Research Council of Canada (NSERC), National Natural Science Foundation of China (Grant Nos. U1909213, 51872209,and 51772219), and Zhejiang Provincial Natural Science Foundation of China (LZ17E02002). The authors also thank Dr. Qunfeng Xiao from Soft X-ray Microcharacterization Beamline (SXRMB) of Canadian Light Source (CLS) for XAS measurements. The CLS is supported by the NSERC, the National Research Council Canada, the Canadian Institutes of Health Research, the Province of Saskatchewan, Western Economic Diversification Canada, and the University of Saskatchewan.

AUTHOR CONTRIBUTIONS

Z.L., H.J., S.W., and Z.C. conceived the idea for the project. Z.L., Y.-P.D., G.L., and G.J. performed electrochemical experiments. D.R., Z.Z., J.Z., R.G., Y.J., D.L., A.M.J., and Y.H. conducted the XRD, XPS, SEM, TEM, and XAS measurements. Z.L., Z.C., Y.Z., D.-H.L., and S.W. discussed the results, analyzed the data, and drafted the manuscript.

DECLARATION OF INTERESTS

The authors declare no competing interest.

Received: May 9, 2020
Revised: June 26, 2020
Accepted: July 21, 2020
Published: August 21, 2020

REFERENCES

Cao, R., Lee, J.-S., Liu, M., and Cho, J. (2012). Recent progress in non-precious catalysts for metal-air batteries. Adv. Energy Mater. *2*, 816–829.

Chen, M., He, Y., Spendelow, J.S., and Wu, G. (2019). Atomically dispersed metal catalysts for oxygen reduction. ACS Energy Lett. *4*, 1619–1633.

Cheng, Y., Dou, S., Veder, J.P., Wang, S., Saunders, M., and Jiang, S.P. (2017). Efficient and durable bifunctional oxygen catalysts based on NiFeO@MnOx core-shell structures for rechargeable Zn-air batteries. ACS Appl. Mater. Interfaces *9*, 8121–8133.

Cheng, Y., He, S., Veder, J.P., De Marco, R., Yang, S.-Z., and Jiang, S.P. (2019a). Atomically dispersed bimetallic FeNi catalysts as highly efficient bifunctional catalysts for reversible oxygen evolution and oxygen reduction reactions. ChemElectroChem *6*, 3478–3487.

Cheng, Y., Wu, X., Veder, J.P., Thomsen, L., Jiang, S.P., and Wang, S. (2019b). Tuning the electrochemical property of the ultrafine metal-oxide nanoclusters by iron phthalocyanine as

efficient catalysts for energy storage and conversion. Energy Environ. Mater. *2*, 5–17.

Cui, H., Jiao, M., Chen, Y.-N., Guo, Y., Yang, L., Xie, Z., Zhou, Z., and Guo, S. (2018). Molten-salt-assisted synthesis of 3D holey N-doped graphene as bifunctional electrocatalysts for rechargeable Zn-air batteries. Small Methods *2*, 1800144.

Deng, Y.P., Jiang, Y., Liang, R., Zhang, S.J., Luo, D., Hu, Y., Wang, X., Li, J.T., Yu, A., and Chen, Z. (2020). Dynamic electrocatalyst with current-driven oxyhydroxide shell for rechargeable zinc-air battery. Nat. Commun. *11*, 1952.

Dou, S., Li, X., Tao, L., Huo, J., and Wang, S. (2016). Cobalt nanoparticle-embedded carbon nanotube/porous carbon hybrid derived from MOF-encapsulated $Co3_O4$ for oxygen electrocatalysis. Chem. Commun. (Camb.) *52*, 9727–9730.

Dou, S., Wang, X., and Wang, S. (2019). Rational design of transition metal-based materials for highly efficient electrocatalysis. Small Methods *3*, 1800211.

Guan, B.Y., Yu, L., and Lou, X.W. (2016). A dual-metal–organic-framework derived electrocatalyst for oxygen reduction. Energy Environ. Sci. *9*, 3092–3096.

He, Y., Hwang, S., Cullen, D.A., Uddin, M.A., Langhorst, L., Li, B., Karakalos, S., Kropf, A.J., Wegener, E.C., Sokolowski, J., et al. (2019). Highly active atomically dispersed CoN4 fuel cell cathode catalysts derived from surfactant-assisted MOFs: carbon-shell confinement strategy. Energy Environ. Sci. *12*, 250–260.

Hou, C.C., Zou, L., and Xu, Q. (2019). A hydrangea-like superstructure of open carbon cages with hierarchical porosity and highly active metal sites. Adv. Mater. *31*, 1904689.

Hu, W., Wang, Y., Hu, X., Zhou, Y., and Chen, S. (2012). Three-dimensional ordered macroporous IrO_2 as electrocatalyst for oxygen evolution reaction in acidic medium. J. Mater. Chem. *22*, 6010–6016.

Huang, Z.F., Song, J., Du, Y., Dou, S., Sun, L., Chen, W., Yuan, K., Dai, Z., and Wang, X. (2019). Optimizing interfacial electronic coupling with metal oxide to activate inert polyaniline for superior electrocatalytic hydrogen generation. Carbon Energy *1*, 77–84.

Huang, Z.-F., Wang, J., Peng, Y., Jung, C.-Y., Fisher, A., and Wang, X. (2017). Design of efficient bifunctional oxygen reduction/evolution electrocatalyst: recent advances and perspectives. Adv. Energy Mater. *7*, 1700544.

Jiang, W.J., Gu, L., Li, L., Zhang, Y., Zhang, X., Zhang, L.J., Wang, J.Q., Hu, J.S., Wei, Z., and Wan, L.J. (2016). Understanding the high activity of Fe-N-C electrocatalysts in oxygen reduction: $Fe/Fe3_C$ nanoparticles boost the activity of Fe-Nx. J. Am. Chem. Soc. *138*, 3570–3578.

Jiang, Y., Deng, Y.-P., Fu, J., Lee, D.U., Liang, R., Cano, Z.P., Liu, Y., Bai, Z., Hwang, S., Yang, L., et al. (2018). Interpenetrating triphase cobalt-based nanocomposites as efficient bifunctional oxygen electrocatalysts for long-lasting rechargeable Zn-air batteries. Adv. Energy Mater. *8*, 1702900.

Lai, C., Wang, J., Lei, W., Xuan, C., Xiao, W., Zhao, T., Huang, T., Chen, L., Zhu, Y., and Wang, D. (2018). Restricting growth of Ni3Fe nanoparticles on heteroatom-doped carbon nanotube/graphene nanosheets as air-electrode electrocatalyst for Zn-air battery. ACS Appl. Mater. Interfaces *10*, 38093–38100.

Lee, J.-S., Nam, G., Sun, J., Higashi, S., Lee, H.-W., Lee, S., Chen, W., Cui, Y., and Cho, J. (2016). Composites of a prussian blue analogue and gelatin-derived nitrogen-doped carbon-supported porous spinel oxides as electrocatalysts for a Zn-air battery. Adv. Energy Mater. *6*, 1601052.

Lee, J.-S., Tai Kim, S., Cao, R., Choi, N.-S., Liu, M., Lee, K.T., and Cho, J. (2011). Metal-air batteries with high energy density: Li-air versus Zn-air. Adv. Energy Mater. *1*, 34–50.

Li, J., Huang, W., Wang, M., Xi, S., Meng, J., Zhao, K., Jin, J., Xu, W., Wang, Z., Liu, X., et al. (2018). Low-crystalline bimetallic metal-organic framework electrocatalysts with rich active sites for oxygen evolution. ACS Energy Lett. *4*, 285–292.

Li, Z., and Yin, L. (2015a). MOF-derived, N-doped, hierarchically porous carbon sponges as immobilizers to confine selenium as cathodes for Li-Se batteries with superior storage capacity and perfect cycling stability. Nanoscale *7*, 9597–9606.

Li, Z., and Yin, L. (2015b). Nitrogen-doped MOF-derived micropores carbon as immobilizer for small sulfur molecules as a cathode for lithium sulfur batteries with excellent electrochemical performance. ACS Appl. Mater. Interfaces *7*, 4029–4038.

Li, Z., and Yin, L. (2018). Efficient gel route to embed phosphorus into MOF-derived porous FePx as anodes for high performance lithium-ion batteries. Energy Storage Mater. *14*, 367–375.

Li, Z., Ge, X., Li, C., Dong, S., Tang, R., Wang, C., Zhang, Z., and Yin, L. (2020). Rational microstructure design on metal–organic framework composites for better electrochemical performances: design principle, synthetic strategy, and promotion mechanism. Small Methods *4*, 1900756.

Li, Z., Li, C., Ge, X., Ma, J., Zhang, Z., Li, Q., Wang, C., and Yin, L. (2016). Reduced graphene oxide wrapped MOFs-derived cobalt-doped porous carbon polyhedrons as sulfur immobilizers as cathodes for high performance lithium sulfur batteries. Nano Energy *23*, 15–26.

Li, Z., Zhang, L., Ge, X., Li, C., Dong, S., Wang, C., and Yin, L. (2017). Core-shell structured CoP/FeP porous microcubes interconnected by reduced graphene oxide as high performance anodes for sodium ion batteries. Nano Energy *32*, 494–502.

Lin, C., Shinde, S.S., Jiang, Z., Song, X., Sun, Y., Guo, L., Zhang, H., Jung, J.-Y., Li, X., and Lee, J.-H. (2017). In situ directional formation of $Co@CoO_x$-embedded 1D carbon nanotubes as an efficient oxygen electrocatalyst for ultra-high rate Zn–air batteries. J. Mater. Chem. A *5*, 13994–14002.

Liu, G., Li, J., Fu, J., Jiang, G., Lui, G., Luo, D., Deng, Y.P., Zhang, J., Cano, Z.P., Yu, A., et al. (2019). An oxygen-vacancy-rich semiconductor-supported bifunctional catalyst for efficient and stable zinc-air batteries. Adv. Mater. *31*, 1806761.

Liu, X., Park, M., Kim, M.G., Gupta, S., Wu, G., and Cho, J. (2015). Integrating NiCo alloys with their oxides as efficient bifunctional cathode catalysts for rechargeable zinc-air batteries. Angew. Chem. Int. Ed. *54*, 9654–9658.

Lu, X.F., Chen, Y., Wang, S., Gao, S., and Lou, X.W.D. (2019). Interfacing manganese oxide and cobalt in porous graphitic carbon polyhedrons boosts oxygen electrocatalysis for Zn-air batteries. Adv. Mater. *31*, 1902339.

Luo, H., Jiang, W.-J., Zhang, Y., Niu, S., Tang, T., Huang, L.-B., Chen, Y.-Y., Wei, Z., and Hu, J.-S. (2018). Self-terminated activation for high-yield production of N,P-codoped nanoporous carbon as an efficient metal-free electrocatalyst for Zn-air battery. Carbon *128*, 97–105.

Luo, M., Yang, Y., Sun, Y., Qin, Y., Li, C., Li, Y., Li, M., Zhang, S., Su, D., and Guo, S. (2019). Ultrathin two-dimensional metallic nanocrystals for renewable energy electrocatalysis. Mater. Today *23*, 45–56.

Meng, J., Niu, C., Xu, L., Li, J., Liu, X., Wang, X., Wu, Y., Xu, X., Chen, W., Li, Q., et al. (2017). General oriented formation of carbon nanotubes from metal-organic frameworks. J. Am. Chem. Soc. *139*, 8212–8221.

Miao, Z., Wang, X., Tsai, M.-C., Jin, Q., Liang, J., Ma, F., Wang, T., Zheng, S., Hwang, B.-J., Huang, Y., et al. (2018). Atomically dispersed Fe-Nx/C electrocatalyst boosts oxygen catalysis via a new metal-organic polymer supramolecule strategy. Adv. Energy Mater. *8*, 1801226.

Mukherjee, S., Cullen, D.A., Karakalos, S., Liu, K., Zhang, H., Zhao, S., Xu, H., More, K.L., Wang, G., and Wu, G. (2018). Metal-organic framework-derived nitrogen-doped highly disordered carbon for electrochemical ammonia synthesis using N2 and $H2_O$ in alkaline electrolytes. Nano Energy *48*, 217–226.

Park, M.G., Lee, D.U., Seo, M.H., Cano, Z.P., and Chen, Z. (2016). 3D ordered mesoporous bifunctional oxygen catalyst for electrically rechargeable zinc-air batteries. Small *12*, 2707–2714.

Qiao, M., Wang, Y., Wang, Q., Hu, G., Mamat, X., Zhang, S., and Wang, S. (2019). Hierarchically ordered porous carbon with atomically dispersed FeN_4 for ultra-efficient oxygen reduction reaction in PEMFC. Angew. Chem. Int. Ed. *59*, 2688–2694.

Ravel, B., and Newville, M. (2005). ATHENA, ARTEMIS, and HEPHAESTUS: data analysis for X-ray absorption spectroscopy using IFEFFIT. J. Synchrotron Radiat. *12*, 537–541.

Tang, C., Wang, B., Wang, H.F., and Zhang, Q. (2017). Defect engineering toward atomic Co-Nx-C in hierarchical graphene for rechargeable flexible solid Zn-air batteries. Adv. Mater. *29*, 1703185.

Tao, L., Lin, C.-Y., Dou, S., Feng, S., Chen, D., Liu, D., Huo, J., Xia, Z., and Wang, S. (2017). Creating coordinatively unsaturated metal sites in metal-organic-frameworks as efficient electrocatalysts for the oxygen evolution reaction: insights into the active centers. Nano Energy *41*, 417–425.

Tsvetkov, N., Lu, Q., Sun, L., Crumlin, E.J., and Yildiz, B. (2016). Improved chemical and electrochemical stability of perovskite oxides with less reducible cations at the surface. Nat. Mater. *15*, 1010–1016.

Wang, M., Lin, M., Li, J., Huang, L., Zhuang, Z., Lin, C., Zhou, L., and Mai, L. (2017a). Metal-organic framework derived carbon-confined $Ni2_P$ nanocrystals supported on graphene for an efficient oxygen evolution reaction. Chem. Commun. *53*, 8372–8375.

Wang, X., Li, Y., Jin, T., Meng, J., Jiao, L., Zhu, M., and Chen, J. (2017b). Electrospun thin-walled $CuCo2_O4$@C nanotubes as bifunctional oxygen electrocatalysts for rechargeable Zn-air batteries. Nano Lett. *17*, 7989–7994.

Wan, X., Wu, R., Deng, J., Nie, Y., Chen, S., Ding, W., Huang, X., and Wei, Z. (2018). A metal-organic framework derived 3D hierarchical Co/N-doped carbon nanotube/nanoparticle composite as an active electrocatalyst for oxygen reduction in alkaline electrolyte. J. Mater. Chem. A *6*, 3386–3390.

Wang, H.-F., Tang, C., and Zhang, Q. (2018a). A review of precious-metal-free bifunctional oxygen electrocatalysts: rational design and applications in Zn−air batteries. Adv. Funct. Mater. *28*, 1803329.

Wang, H.-F., Tang, C., Wang, B., Li, B.-Q., Cui, X., and Zhang, Q. (2018b). Defect-rich carbon fiber electrocatalysts with porous graphene skin for flexible solid-state zinc–air batteries. Energy Storage Mater. *15*, 124–130.

Wang, J., Gan, L., Zhang, W., Peng, Y., Yu, H., Yan, Q., Xia, X., and Wang, X. (2018c). In situ formation of molecular Ni-Fe active sites on heteroatom-doped graphene as a heterogeneous electrocatalyst toward oxygen evolution. Sci. Adv. *4*, eaap7970.

Wang, X.X., Cullen, D.A., Pan, Y.T., Hwang, S., Wang, M., Feng, Z., Wang, J., Engelhard, M.H., Zhang, H., He, Y., et al. (2018d). Nitrogen-coordinated single cobalt atom catalysts for oxygen reduction in proton exchange membrane fuel cells. Adv. Mater. *30*, 1606459.

Wang, X., Yu, L., Guan, B.Y., Song, S., and Lou, X.W.D. (2018e). Metal-organic framework hybrid-assisted formation of Co_3O_4/Co-Fe oxide double-shelled nanoboxes for enhanced oxygen evolution. Adv. Mater. *30*, 1801211.

Wang, Z., Lu, Y., Yan, Y., Larissa, T.Y.P., Zhang, X., Wuu, D., Zhang, H., Yang, Y., and Wang, X. (2016). Core-shell carbon materials derived from metal-organic frameworks as an efficient oxygen bifunctional electrocatalyst. Nano Energy *30*, 368–378.

Wu, Y., Jiang, G., Liu, G., Lui, G., Cano, Z.P., Li, Q., Zhang, Z., Yu, A., Zhang, Z., and Chen, Z. (2019). A 3D ordered hierarchically porous non-carbon electrode for highly effective and efficient capacitive deionization. J. Mater. Chem. A *7*, 15633–15639.

Xia, B.Y., Yan, Y., Li, N., Wu, H.B., Lou, X.W., and Wang, X. (2016). A metal-organic framework-derived bifunctional oxygen electrocatalyst. Nat. Energy *1*, 15006.

Xu, H., Cao, J., Shan, C., Wang, B., Xi, P., Liu, W., and Tang, Y. (2018). MOF-derived hollow CoS decorated with CeOx nanoparticles for boosting oxygen evolution reaction electrocatalysis. Angew. Chem. Int. Ed. *57*, 8654–8658.

Xu, L., Jiang, Q., Xiao, Z., Li, X., Huo, J., Wang, S., and Dai, L. (2016). Plasma-engraved $Co3_O4$ nanosheets with oxygen vacancies and high surface area for the oxygen evolution reaction. Angew. Chem. Int. Ed. *55*, 5277–5281.

Xuan, C., Lei, W., Wang, J., Zhao, T., Lai, C., Zhu, Y., Sun, Y., and Wang, D. (2019). Sea urchin-like Ni-Fe sulfide architectures as efficient electrocatalysts for the oxygen evolution reaction. J. Mater. Chem. A *7*, 12350–12357.

Yan, D., Li, Y., Huo, J., Chen, R., Dai, L., and Wang, S. (2017). Defect chemistry of nonprecious-metal electrocatalysts for oxygen reactions. Adv. Mater. *29*, 1606459.

Yang, M., Hu, X., Fang, Z., Sun, L., Yuan, Z., Wang, S., Hong, W., Chen, X., and Yu, D. (2017). Bifunctional MOF-derived carbon photonic crystal architectures for advanced Zn-air and Li-S batteries: highly exposed graphitic nitrogen matters. Adv. Funct. Mater. *27*, 1701971.

Yin, J., Li, Y., Lv, F., Fan, Q., Zhao, Y.Q., Zhang, Q., Wang, W., Cheng, F., Xi, P., and Guo, S. (2017). NiO/CoN porous nanowires as efficient bifunctional catalysts for Zn-air batteries. ACS Nano *11*, 2275–2283.

Yuan, Y., Zhan, C., He, K., Chen, H., Yao, W., Sharifi-Asl, S., Song, B., Yang, Z., Nie, A., Luo, X., et al. (2016). The influence of large cations on the electrochemical properties of tunnel-structured metal oxides. Nat. Commun. *7*, 13374.

Zhang, H., Nai, J., Yu, L., and Lou, X.W. (2017). Metal-organic-framework-based materials as platforms for renewable energy and environmental applications. Joule *1*, 77–107.

Zhang, J., Jiang, G., Cumberland, T., Xu, P., Wu, Y., Delaat, S., Yu, A., and Chen, Z. (2019a). A highly sensitive breathable fuel cell gas sensor with nanocomposite solid electrolyte. InfoMat *1*, 234–241.

Zhang, Z., Deng, Y.P., Xing, Z., Luo, D., Sy, S., Cano, Z.P., Liu, G., Jiang, Y., and Chen, Z. (2019b). "Ship in a bottle" design of highly efficient bifunctional electrocatalysts for long-lasting rechargeable Zn-air batteries. ACS Nano *13*, 7062–7072.

Zhong, Y., Lu, Q., Zhu, Y., Zhu, Y., Zhou, W., Wang, S., and Shao, Z. (2017). Fructose-derived hollow carbon nanospheres with ultrathin and ordered mesoporous shells as cathodes in lithium-sulfur batteries for fast energy storage. Adv. Sustain. Syst. *1*, 1700081.

Zhong, Y., Xu, X., Wang, W., and Shao, Z. (2018). Recent advances in metal-organic framework derivatives as oxygen catalysts for zinc-air batteries. Batter. Supercaps *2*, 272–289.

iScience, Volume *23*

Supplemental Information

Deep-Breathing Honeycomb-like Co-N_x-C Nanopolyhedron Bifunctional Oxygen Electrocatalysts for Rechargeable Zn-Air Batteries

Zhaoqiang Li, Gaopeng Jiang, Ya-Ping Deng, Guihua Liu, Dezhang Ren, Zhen Zhang, Jianbing Zhu, Rui Gao, Yi Jiang, Dan Luo, Yanfei Zhu, Dai-Huo Liu, Altamash M. Jauhar, Huile Jin, Yongfeng Hu, Shun Wang, and Zhongwei Chen

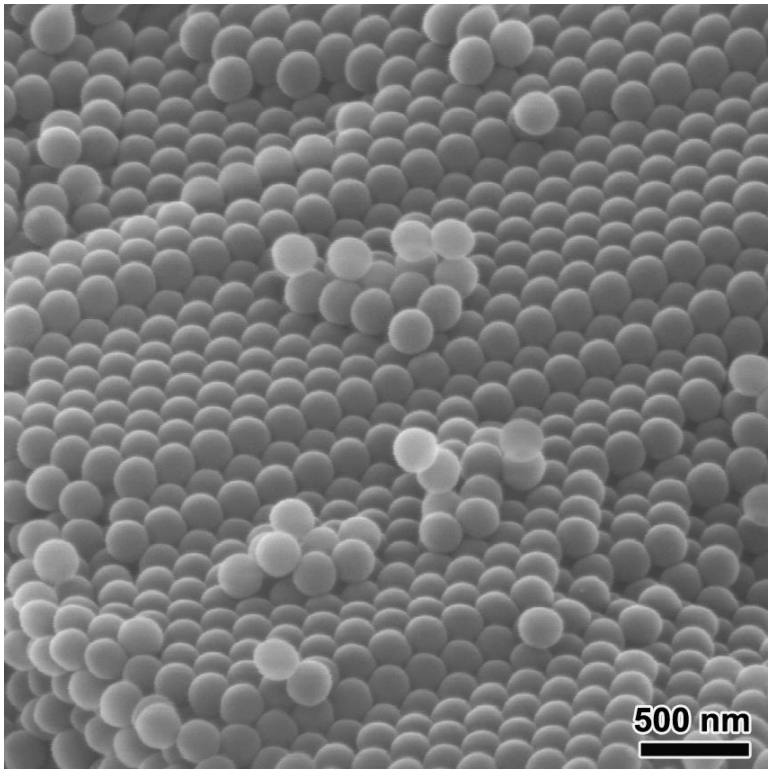

Figure S1. SEM image of the well-stacked PS template. Related to Figure 1.

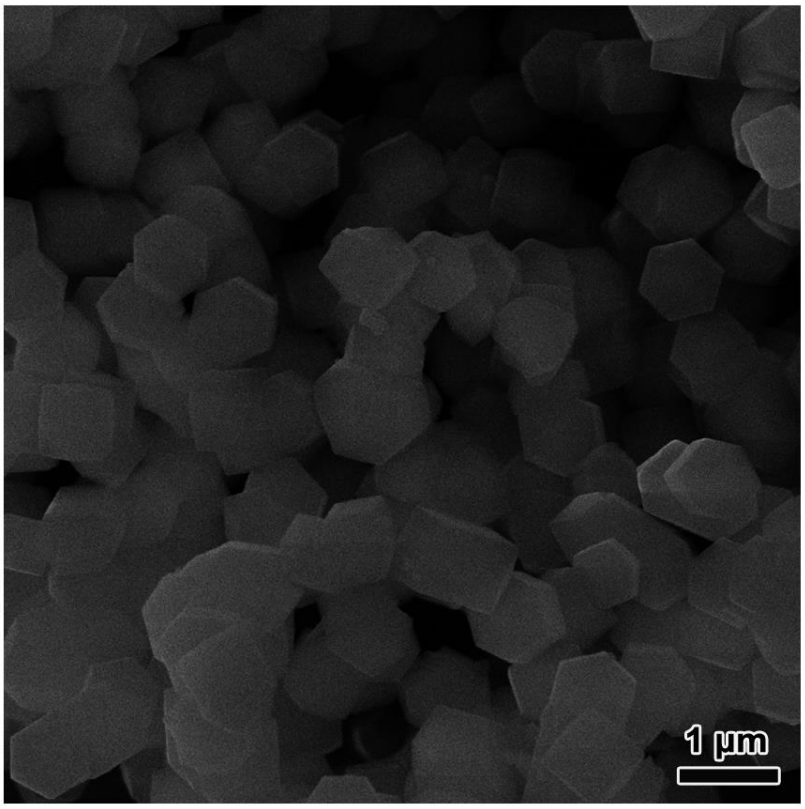

Figure S2. SEM image of the bulk ZIF-67. Related to Figure 2.

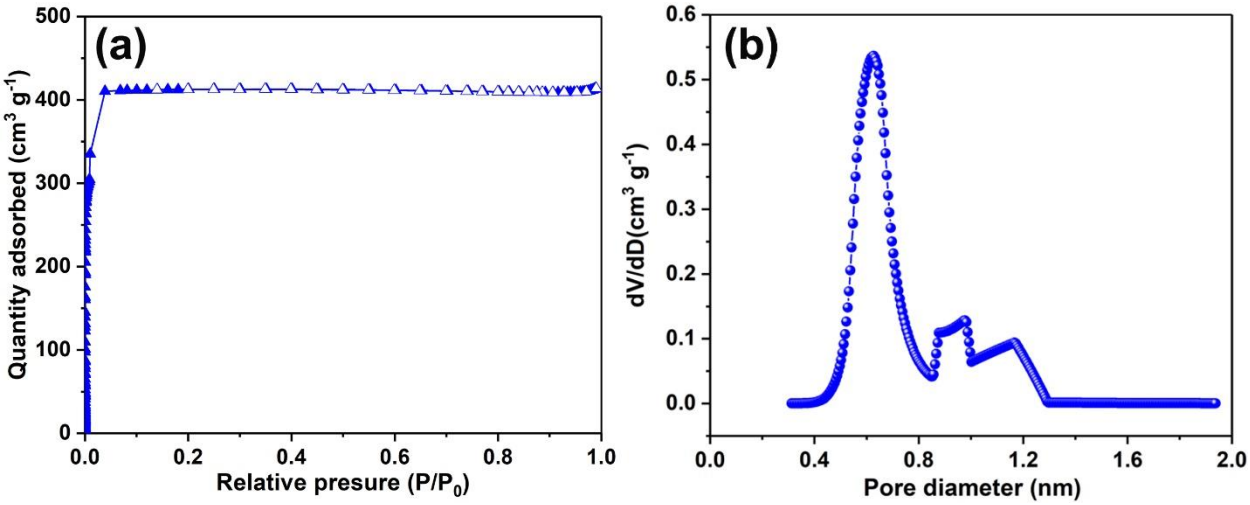

Figure S3. (a) N_2 adsorption-desorption isotherms and (b) pore size distributions of the bulk ZIF-67. Related to Figure 2.

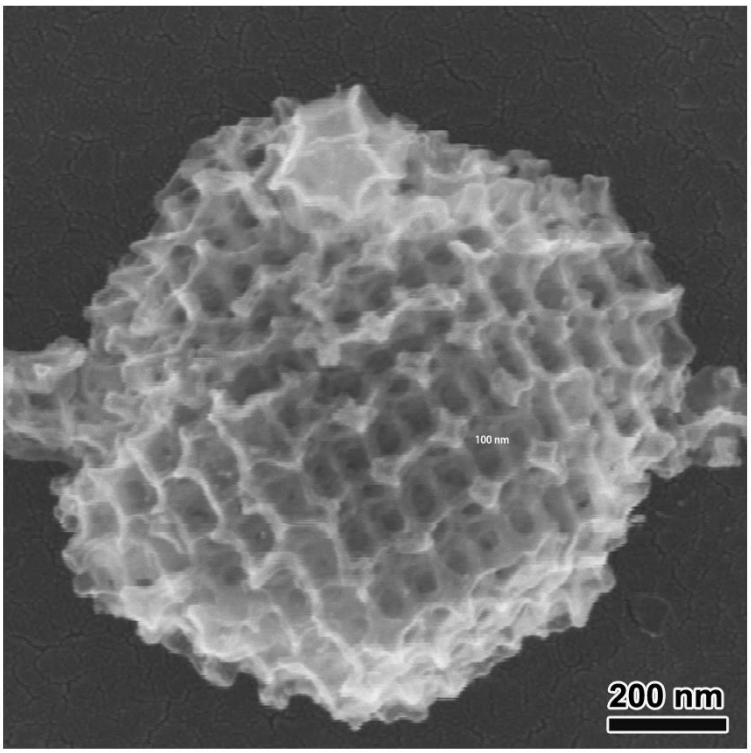

Figure S4. SEM images of the Honeycomb-600. Related to Figure 3.

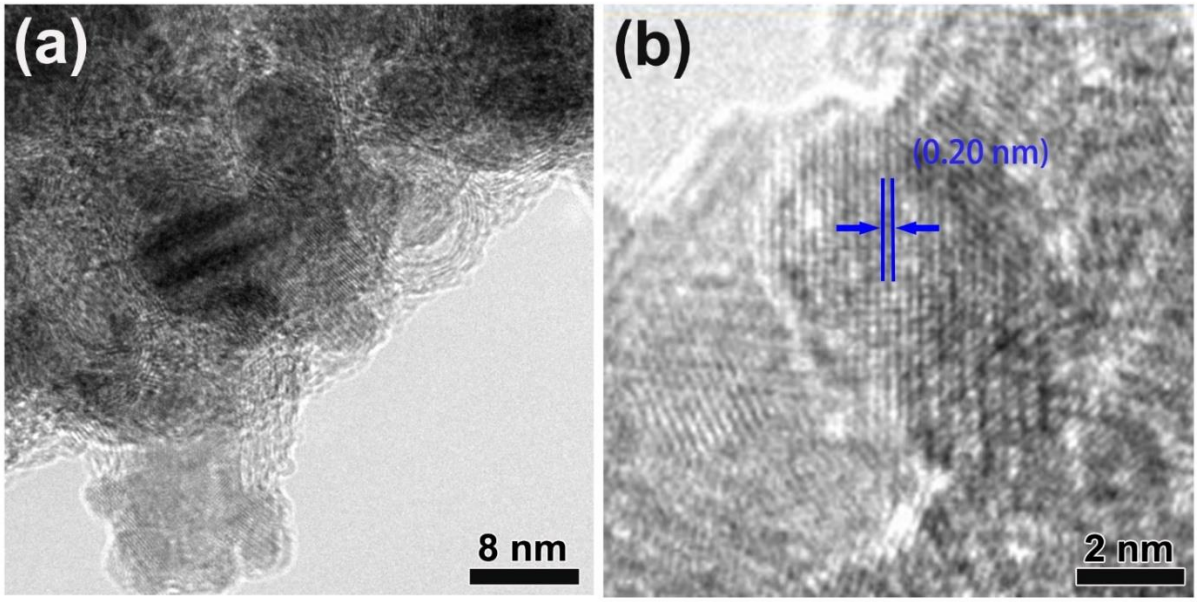

Figure S5. (a, b) TEM images of the Honeycomb-600. Related to Figure 3.

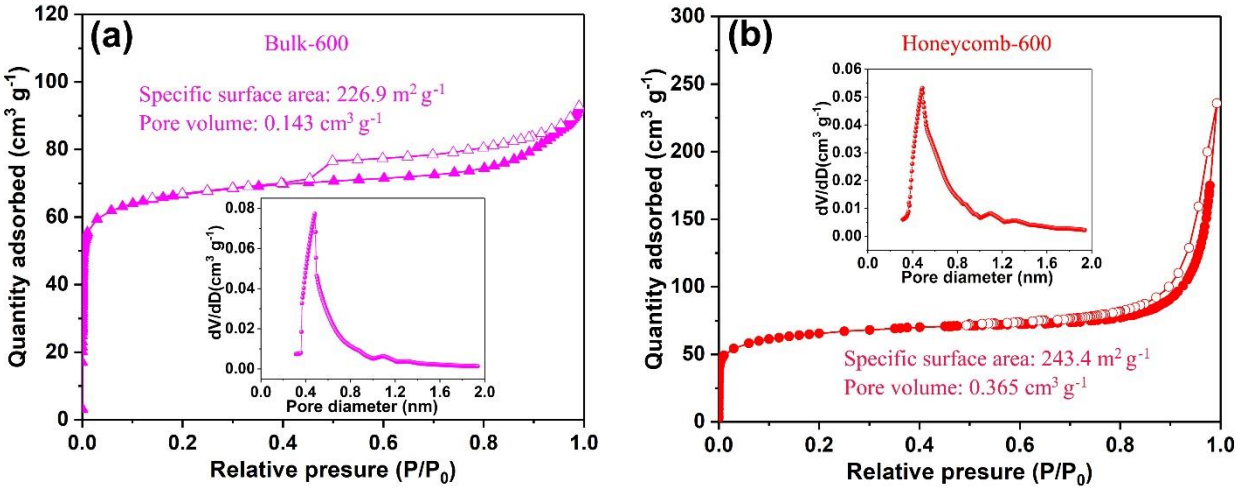

Figure S6. N_2 adsorption-desorption isotherms and pore size distributions of (a) Bulk-600 and (b) Honeycomb-600. Related to Figure 3.

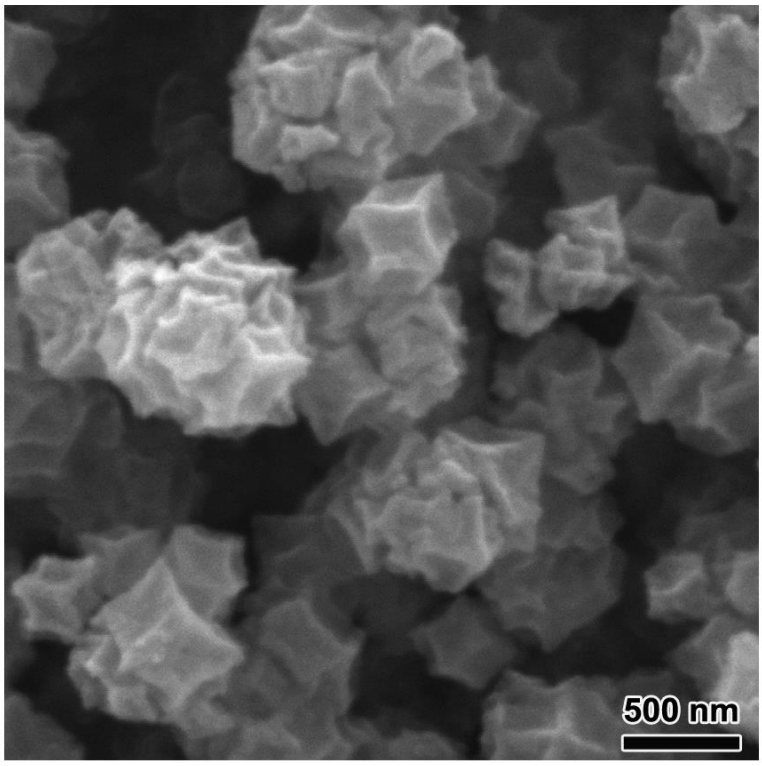

Figure S7. SEM images of the Bulk-600. Related to Figure 3.

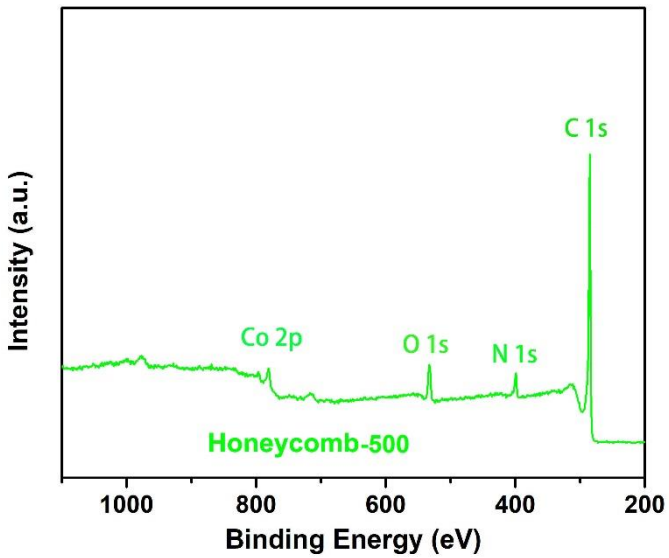

Figure S8. XPS survey spectrum of the Honeycomb-500. Related to Figure 4.

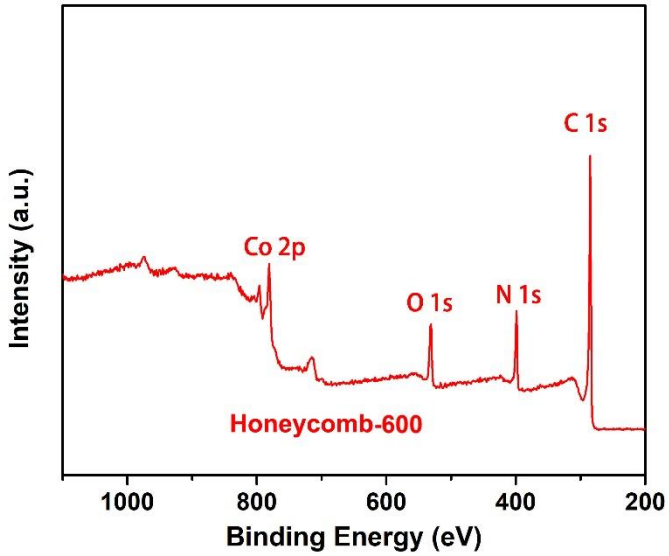

Figure S9. XPS survey spectrum of the Honeycomb-600. Related to Figure 4.

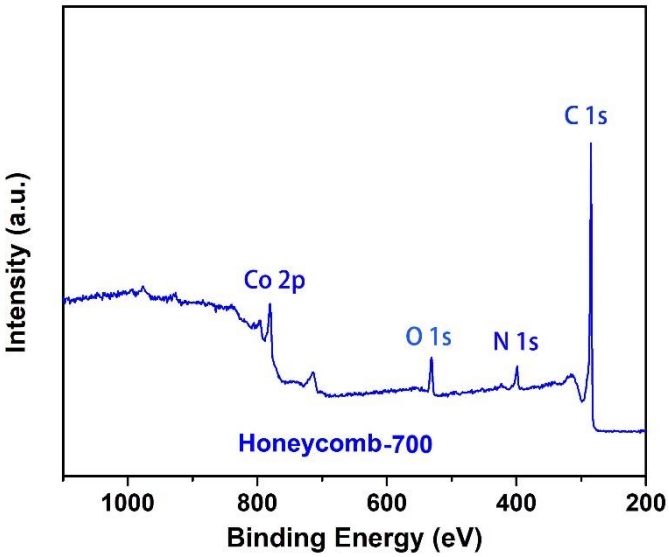

Figure S10. XPS survey spectrum of the Honeycomb-700. Related to Figure 4.

Table S1. Elemental compositions calculated from XPS results. Related to Figure 4.

	C	N	O	Co
Honeycomb-500	85.36 at%	6.43 at%	6.72 at%	1.48 at%
Honeycomb-600	73.5 at%	13.58 at%	9.12 at%	3.79 at%
Honeycomb-700	83.99 at%	6.35 at%	6.87 at%	2.79 at%

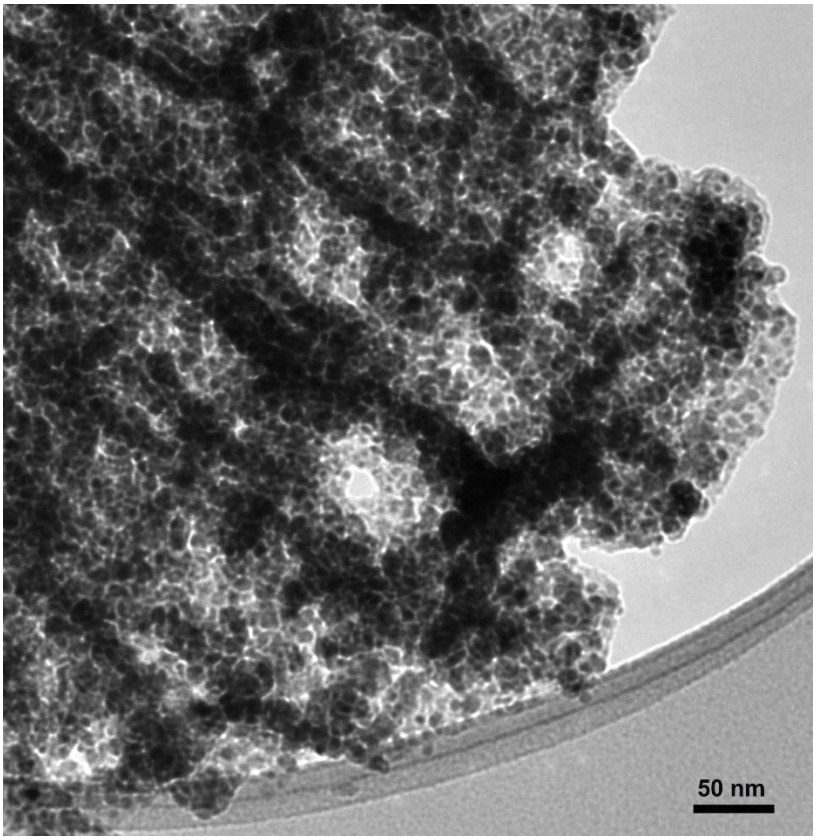

Figure S11. TEM image of the Honeycomb-700. Related to Figure 5.

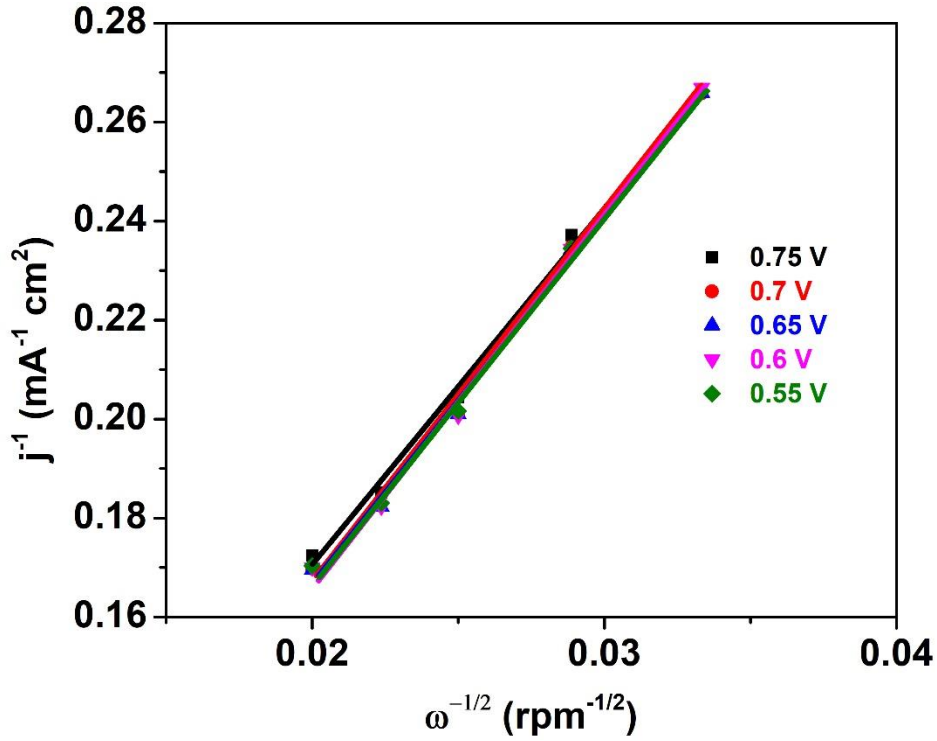

Figure S12. K-L plots obtained at different potentials. Related to Figure 5.

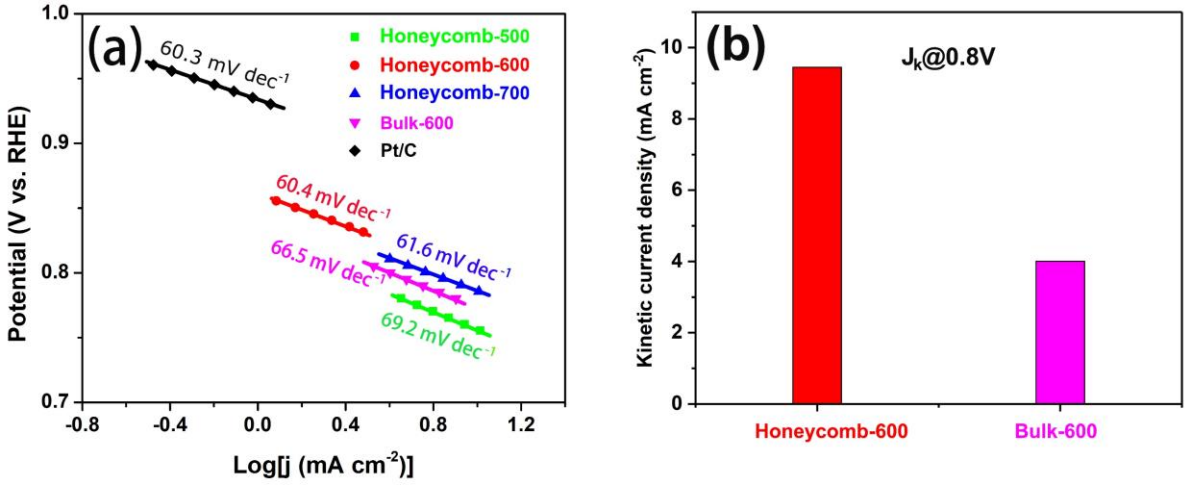

Figure S13. (a) ORR Tafel slopes in 0.1 M KOH solution. (b) Kinetic current densities (J_k) of Honeycomb-600 and Bulk-600 samples at 0.8 V. Related to Figure 5.

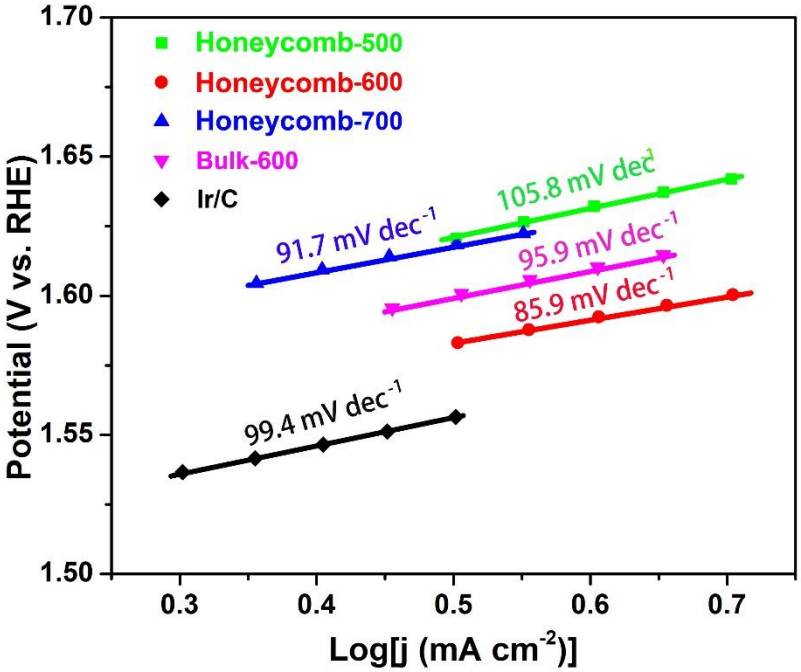

Figure S14. OER Tafel slopes of various electrodes in 0.1 M KOH solution. Related to Figure 5.

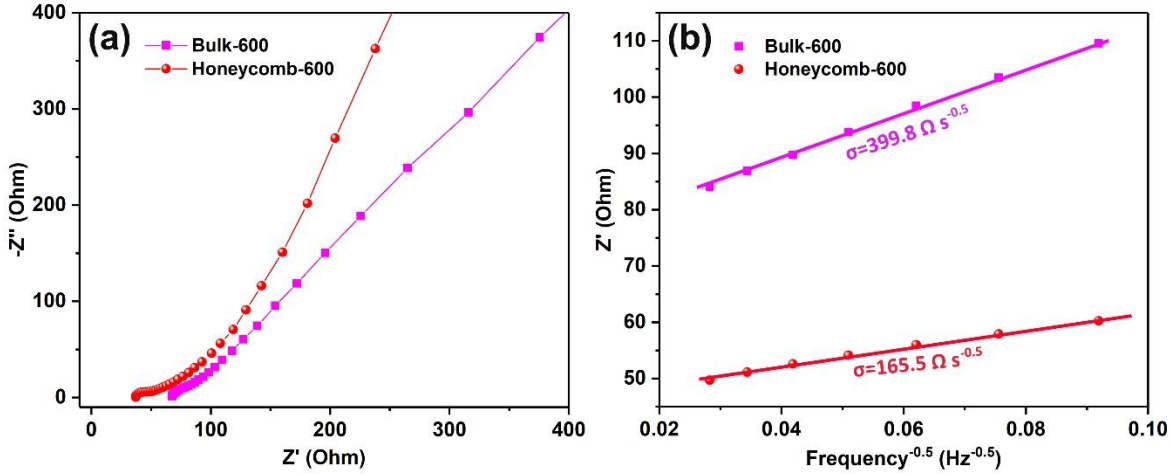

Figure S15. EIS results of the Bulk-600 and Honeycomb-600 samples. (a) Nyquist plots and (b) linear fitting to Z' versus $\omega^{-0.5}$ plots. Related to Figure 5.

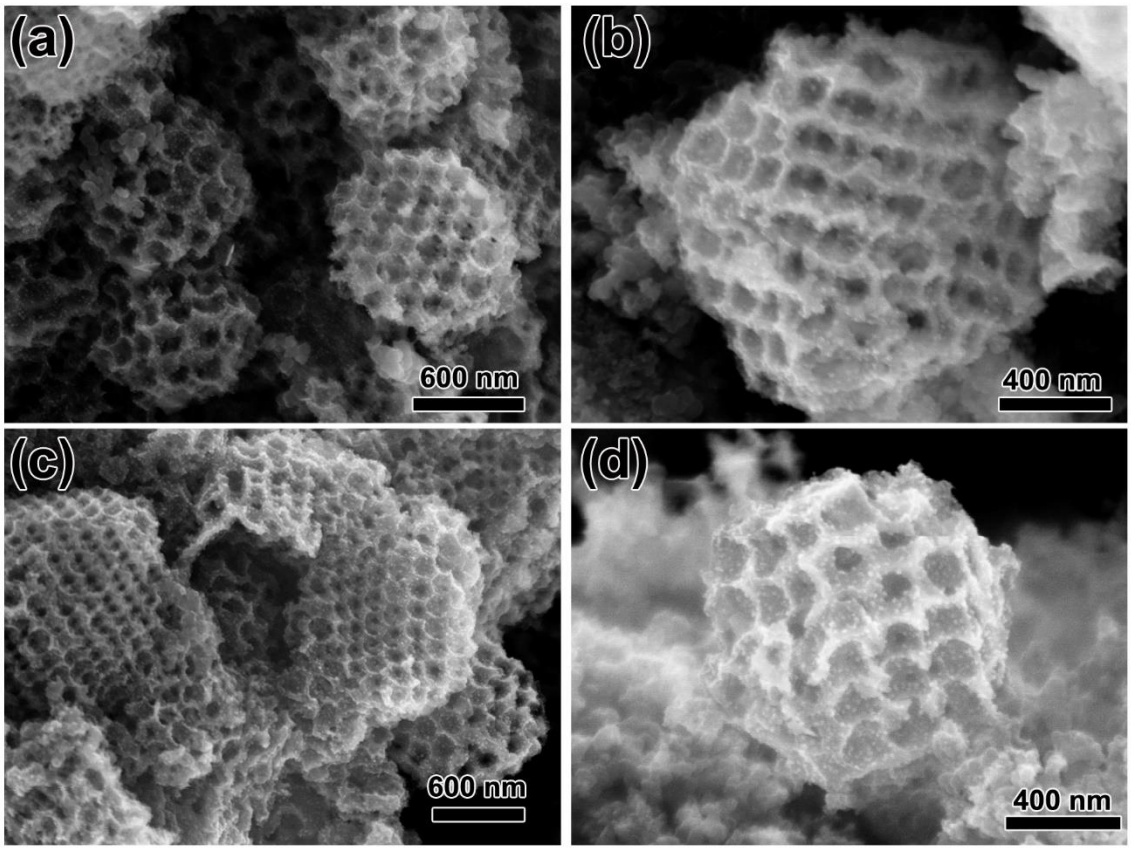

Figure S16. SEM images of Honeycomb-600 after (a, b) ORR and (c, d) OER durability tests. Related to Figure 5.

Transparent Methods

Chemicals: 15 wt. % Nafion in isopropanol was purchased from Ion Power Inc. Zinc acetate tetrahydrate (99%), cobalt nitrite hexahydrate (99%), methanol (99.9%), 2-Methylimidazole (99%), potassium persulfate (99.99%), Styrene (99%), polyvinylpyrrolidone (average mol wt 40,000), ethanol (99.9%) potassium hydroxide (85%) and N, N-Dimethylformamide (99.99%) were bought from Sigma–Aldrich.

Synthesis of Polystyrene (PS) template: The monodispersed polystyrene (PS) spheres were firstly synthesized using an emulsion polymerization reaction. First, de-ionized water was boiled for 5 minutes and then cooling down for further use. 2.5 g polyvinylpyrrolidone (PVP) was dissolved into 200 ml boiled water in a three-neck flask and then were reflux in oil bath under 70 °C for 15 minutes. The three-neck flask was filled with N_2 during the subsequent polymerization process. 24 ml styrene monomer was then added into the PVP solution and stirred for 15 minutes. The 40 ml aqueous solution containing 0.2 potassium persulfate was then added into the above mixture dropwise. The PS solution was finally obtained after reaction for 24h under 70 °C in oil bath. The PS template was constructed by centrifuging the PS solution under 3500 rpm for 16 h.

Synthesis of honeycomb-like ZIF-67 and normal solid ZIF-67: The PS template bulk was then immersed into 1.2 M cobalt nitrate ethanol solution for 1h, which was followed by 20 minutes vacuum treatment before taking out. After drying in electric oven under 50 °C overnight, the obtained PS/$Co(NO_3)_2$ was then immersed into 3.6 M 2-mim methanol solution. Before aging for 24 h for the nucleation of ZIF-67 crystals, the system firstly underwent a vacuum treatment of 10 min with the purpose of 2-mim solution infusing inside the PS template. The PS/ZIF-67 was then soaked in DMF to remove PS spheres, finally obtaining honeycomb-like ZIF-67. For the synthesis of normal solid ZIF-67, the 9.96 g cobalt nitrite hexahydrate and 13.12 g 2-Methylimidazole were dissolved into 1 L methanol, respectively. Then the cobalt nitrite solution was poured into 2-Methylimidazole solution with vigorous stirring for 1 minute. After aging for 24 h, the ZIF-67 was collected by centrifuge, which was then washed with ethanol and dried for further use.

Synthesis of honeycomb-like Co-N_x-C: The honeycomb-like ZIF-67 or normal ZIF-67 was loaded into a quartz boat and annealed at 420 °C for 6 h with a heating rate of 2 °C/minute under Ar atmosphere, then arising to 500, 600 or 700 °C with a heating rate of 5 °C/minute. The atmosphere was then changed to NH_3 and maintained for 50 minutes. After cooling down to room temperature, the honeycomb-like Co-N_x-C or normal Co-N_x-C were obtained.

Fabrication of Zn-Air Battery: Typically, Zinc-Air battery was assembled by employing zinc plate as anode, electrocatalyst containing gas diffusion layer as air electrode, aqueous solution containing 6 M KOH and 0.2 M $Zn(CH_3COO)_2$ as electrolyte. For the fabrication of air electrode, the isopropanol ink containing electrocatalysts, Vulcan XC 72 and nafion was homogenously sprayed onto a carbon paper with a catalyst loading of 1 mg cm^{-2}. For comparison, the commercial Pt/C+Ir/C with a weight ratio of (1:1) was also employed to fabricate a GDL as benchmarks.

Materials Characterization: SEM images was taken from a Zeiss Leo 1530 and TEM using a Zeiss Libra 200MC. XRD patterns were measured using a Rigaku MiniFlex 600 X-ray diffractometer. The pore structure and specific surface areas were calculated by using a Micromertics ASAP 2020 analyzer. The XPS spectra was tested on a Thermal Scientific K-Alpha XPS spectrometer. Co K-edge XANES spectra were obtained from the SXR-B beamline at Canadian Light Source Inc, Canada.

Electrochemical measurements: The electrocatalytic performance was tested in a three-electrode system using a Biologic VMP-3 electrochemical workstation. The CV and LSV curves were measured on a rotating disk electrode (RDE) in a three-electrode cell, which contains a saturated calomel electrode as reference electrode, a glassy carbon (GC) electrode or Gold electrode as working electrode and a graphite rod as counter electrode and the calibration to the RHE is calculated the Nernst equation: $E_{RHE} = E_{SCE} + 0.059 \times pH + 0.241$. The electrocatalyst ink was prepared by adding 3 mg catalyst, 1 mg Vulcan XC 72 into

750 µl 0.1 wt% Nafion isopropanol solution followed with ultrasonication for 30 minutes. Then 15 µl ink was pipetted onto GC or Gold electrode to achieve a loading of 0.3 mg cm^{-2}. The LSV curves were obtained with a scan rate of 5 mV s^{-1} in 0.1 M KOH. The polarization curves were obtained by using a galvanodynamic method with a scan rate of 1 mA s^{-1}. The OER and ORR stability tests were conducted by dip coating of electrocatalysts inks onto carbon paper to achieve a mass loading of 0.5 mg cm^{-2}, which were then employed as working electrode in a three-electrode system to conduct OER or ORR chronoamperometric tests. The electron transfer number is calculated from the K-L equation: $1/j=1/j_k+1/(B\omega^{1/2})$. A LAND CT2001A battery testing machine was employed for galvanostatic charging/discharging tests. EIS was conducted by Biologic VMP-3 electrochemical workstation with the frequency range of 0.1 Hz-100 kHz.